

A functional approach for curve alignment and shape analysis

Moindjié, Issam-Ali^{1,*}, Beaulac, Cédric¹, and Descary, Marie-Hélène¹

¹Department of mathematics, Université du Québec à Montréal

*Corresponding author: moindjie.issam-ali@uqam.ca

Abstract

The shape $\tilde{\mathbf{X}}$ of a random planar curve \mathbf{X} is what remains after removing deformation effects such as scaling, rotation, translation, and parametrization. Previous studies in statistical shape analysis have focused on analyzing $\tilde{\mathbf{X}}$ through discrete observations of the curve \mathbf{X} . While this approach has some computational advantages, it overlooks the continuous nature of both \mathbf{X} and its shape $\tilde{\mathbf{X}}$. It also ignores potential dependencies among the deformation variables and their effect on $\tilde{\mathbf{X}}$, which may result in information loss and reduced interpretability. In this paper, we introduce a novel framework for analyzing \mathbf{X} in the context of Functional Data Analysis (FDA). Basis expansion techniques are employed to derive analytic solutions for estimating the deformation variables such as rotation and reparametrization, thereby achieving shape alignment. The generative model of \mathbf{X} is then investigated using a joint-principal component analysis approach. Numerical experiments on simulated data and the *MPEG-7* database demonstrate that our new approach successfully identifies the deformation parameters and captures the underlying distribution of planar curves in situations where traditional FDA methods fail to do so.

1 Introduction

The analysis of images has become increasingly important with advances in storage and acquisition technologies, making them widely used in the scientific and industrial domains. Representing images as matrices, where each pixel encodes grayscale intensity or RGB values, has enabled modern deep learning methods to achieve outstanding performances for several learning tasks, including generative modeling (see e.g. Oussidi and Elhassouny (2018) for a review). However, this matrix-based representation does not explicitly capture the main aspect of images: the objects they depict are characterized by their *shapes* and textures. This is a major drawback, as the estimation of image distributions is done through an extremely opaque architecture and at a high computational cost, making these methods unsuitable for interpretable analyses or learning with few observations.

To address this issue, we propose shifting the focus from pixel-based analysis to the study of shapes represented in images. In particular, we focus on the silhouette \mathbf{X} , which

represents the envelope or contour of the main object in the image. This variable can be seen as a random parametric planar curve:

$$\mathbf{X}(t) = \begin{pmatrix} X^{(1)}(t) \\ X^{(2)}(t) \end{pmatrix},$$

where $t \in [0, 1]$ represents the proportion of the curve that has been traveled from the start ($t = 0$) to the end ($t = 1$) and $X^{(1)}$, $X^{(2)}$ are the coordinate functions. Moreover, if the contour of the image is closed, then we have $\mathbf{X}(0) = \mathbf{X}(1)$; we focus on this setup in this work. Figure 1 illustrates the pipeline for extracting the planar curve \mathbf{X} from an image.

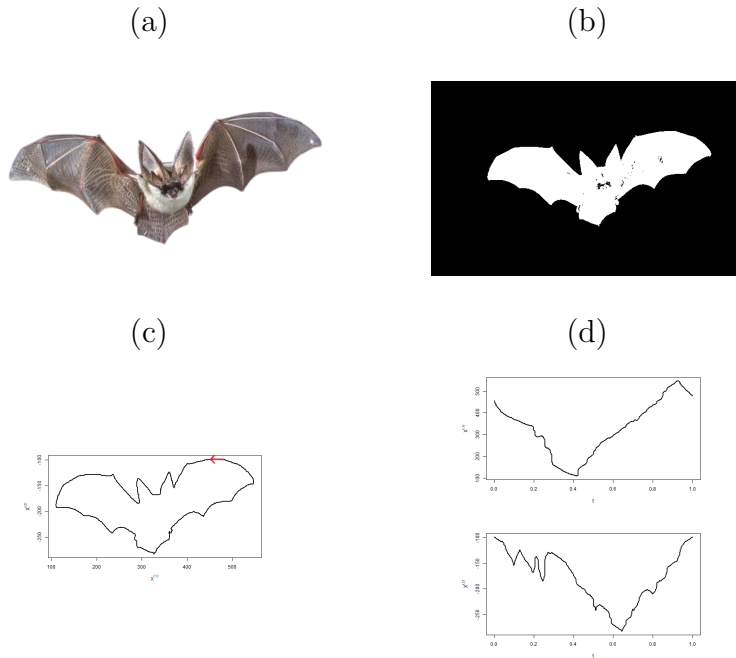


Figure 1: From an image to the planar curve \mathbf{X} : (a) original image (nl, 2020), (b) binarized image, (c) contour of the object in the image, and (d) the coordinate functions $X^{(1)}(t)$ and $X^{(2)}(t)$. The red arrow in (c) indicates the starting point and the orientation of the traveling used to obtain the coordinate functions in (d).

The random planar curve \mathbf{X} is assumed to be the deformed version of a latent variable $\tilde{\mathbf{X}}$:

$$\mathbf{X}(t) = \rho \mathbf{O} \tilde{\mathbf{X}} \circ \gamma(t) + \mathbf{T}, \quad t \in [0, 1], \quad (1)$$

where $(\rho, \mathbf{O}, \mathbf{T}, \gamma)$ are the deformation variables and $\tilde{\mathbf{X}}$ is the *shape* of \mathbf{X} in the sense of Kendall (1989), i.e., what remains when all deformations are discarded. The deformation variables transform $\tilde{\mathbf{X}}$ to \mathbf{X} by the action of scaling ($\rho \in \mathbb{R}^+$), translating ($\mathbf{T} \in \mathbb{R}^2$), rotating ($\mathbf{O} \in SO(2)$) and reparametrizing ($\gamma \in \Gamma$, where Γ is a space of reparametrization functions from $[0, 1] \rightarrow [0, 1]$).

Studying \mathbf{X} has been the matter of the shape analysis community. They usually consider a collection of discrete observations along the curve \mathbf{X} . In early work, scientists chose this finite number of points and saw them as "landmarks", i.e., points of correspondence on

each object that match between and within populations (Dryden and Mardia, 1998). These approaches neglect the continuity of the contour’s object and introduce subjectivity while choosing the landmarks. Modern approaches consider \mathbf{X} as a planar curve (see e.g Younes (1998)). In this case, the authors of Srivastava et al. (2010) and Srivastava and Klassen (2016) have established a flexible framework based on elastic distance ideas to study $\tilde{\mathbf{X}}$ with observations of \mathbf{X} , assuming that deformation variables are nuisance. In estimating γ and the rotation matrix \mathbf{O} , they used discrete observations of \mathbf{X} through a dynamical programming approach. This method also leads to an arbitrary choice: which points should be considered in the algorithm.

In this paper, we propose a functional data approach to study the random planar curve defined in equation (1). In particular, \mathbf{X} is seen as a bi-variate functional variable taking values in $\mathcal{H} = L^2([0, 1]) \times L^2([0, 1])$, where $L^2([0, 1])$ is the set of squared integrable functions. Realizations of the variable \mathbf{X} are then functional data.

Functional Data Analysis (FDA) has been an active research domain in statistics since the pioneering work of Ramsey and Silverman (2005). Random shapes form a particular class of functional data that lie in a non-linear manifold. In Stöcker et al. (2023), the authors studied them as covariates in generalized additive regression models. However, the set of deformations considered that act on $\tilde{\mathbf{X}}$ does not include reparametrization functions. Some research has specifically examined the distribution of shape variables within the FDA framework (see e.g Dai and Müller (2018), Dai (2022)). Nevertheless, to the knowledge of the authors, the problem of jointly estimating all the deformation variables and proposing a model for \mathbf{X} has not been explicitly addressed in the FDA community.

A naive approach would be to ignore all these specificities and consider \mathbf{X} solely as a multivariate functional variable. This assumes that the variable we study is a vector of $d \geq 2$ dimensions, where each component $X^{(j)}$ is a functional random variable for $j = 1, \dots, d$. However, using this prism might be ineffective in correctly estimating the generative distribution of \mathbf{X} since most methodologies rely on linear approaches, such as multivariate functional principal component analysis (see e.g. Happ and Greven (2018), Jacques and Preda (2014)).

For illustration purposes, Figure 2 depicts realizations of \mathbf{X} and their sample mean. The left column displays planar curves, while the corresponding coordinate functions are shown in the middle and right columns. The first row presents a sample of $n = 10$ "heart" planar curves exhibiting variations in rotation and reparametrization and the second row shows the estimate of the mean function $\mathbb{E}(\mathbf{X}) \in \mathcal{H}$ which is defined by its coordinate-wise expectation:

$$\mathbb{E}(\mathbf{X}(t)) = (\mathbb{E}(X^{(1)}(t)) \quad \mathbb{E}(X^{(2)}(t)))^\top.$$

As illustrated in the figure, this definition fails to preserve the "heart" silhouette. This highlights the issue of applying linear approach directly to the planar curves.

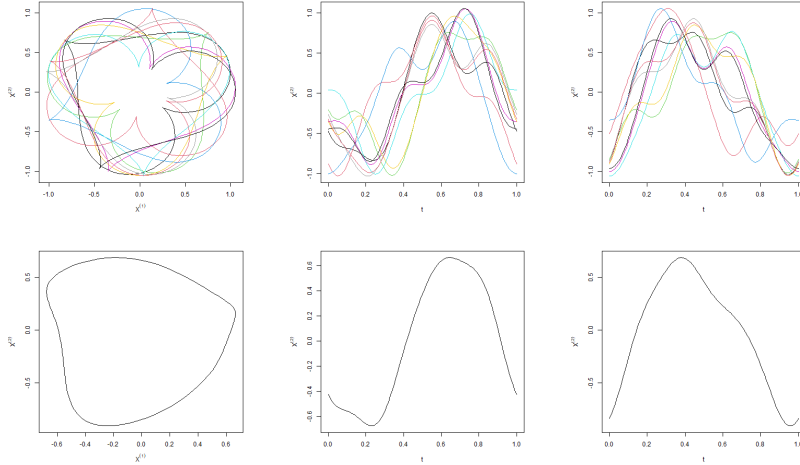


Figure 2: Examples of observations of \mathbf{X} (first row) and their sample mean (second row). Columns present the planar curves, the first and the second coordinate functions, respectively.

A similar problem occurs when alignment is not addressed for a univariate functional variable X taking values in $L^2([0, 1])$. In this case, X can be expressed as:

$$X = \tilde{X} \circ \gamma,$$

where γ is a warping function and \tilde{X} represents the curve without phase variation. Hence, obtaining the shape $\tilde{\mathbf{X}}$ from \mathbf{X} can be viewed as a generalization of the alignment procedure for univariate functional variables to the bivariate case. In the univariate case, this problem has been the source of many developments in FDA (see Chap.7 in Ramsey and Silverman (2005) and Marron et al. (2015) for a review). For example, in Tucker et al. (2013) a flexible generative model of X is proposed. This method relies on a joint functional principal component analysis of bijective transformations of \tilde{X} and γ , inspired by the square-root velocity framework. Using a transformation of $\gamma \in \Gamma$ is mandatory due to the complex structure of Γ , defined in this case as a space of diffeomorphism functions. Happ et al. (2019) discuss several choices of transformations, comparing their relative advantages and drawbacks. They found that square-root velocity inverse transformations might lead to warping functions with atypical structures, making them hard to interpret.

In this paper, we consider the following space of reparametrization functions

$$\Gamma = \{\gamma_\delta(t) = \text{mod}(t - \delta, 1), t \in [0, 1], \delta \in [0, 1]\}, \quad (2)$$

where $\text{mod}(\cdot, 1)$ is the modulo 1 function. It is thus assumed that each reparametrization function is uniquely characterized by its "starting point" $\delta \in [0, 1]$. The motivation for choosing this particular space is discussed in Section 2.1.

An appealing aspect of considering the space Γ defined in (2) is that when representing the planar curve \mathbf{X} as a finite Fourier series, the estimation of the reparametrization function and the rotation matrix can be reformulated as an optimization program related to the Procrustes problem (Schönemann, 1966). Although Fourier functions have been the source

of several investigations in the shape analysis community to summarize the shape (see e.g. Chap.6 in Burger and Burge (2009)), our approach proposes a novel framework that uses these functions to define a basis expansion. Indeed, in the spirit of functional data analysis, they are used to recover the functional form of each discretely observed realization of \mathbf{X} .

In summary, the main contributions of this work are as follows:

- A functional data-based procedure to estimate the deformation variables from a bivariate random planar curve \mathbf{X} . This method exploits the propriety of the Fourier basis functions coupled with the set of reparametrization functions when the variations are consequences of different starting points.
- A novel modelization for \mathbf{X} that explicitly accounts for the deformation variables through a joint principal component analysis (PCA): one is done on the aligned functional variable ($\rho\tilde{\mathbf{X}}$) and the other on the remaining deformation variables.

The remainder of the paper is organized as follows. Section 2 focuses on estimating the deformation variables while Section 3 introduces a generative model for \mathbf{X} . Numerical experiments on simulated data are presented in Section 4 followed by an application of our approach to the *MPEG-7* database in Section 5. Finally, the paper concludes with a discussion in Section 6. The appendix contains additional figures related to the real data analysis of Section 5 and proofs of the theoretical results.

2 Alignment of planar closed curves

Let \mathbf{X} be a functional variable taking values in $\mathcal{H} = L^2([0, 1]) \times L^2([0, 1])$, such that $\mathbf{X}(0) = \mathbf{X}(1)$, and defined as in model (1). Note that \mathcal{H} is a Hilbert space with the inner product $\langle \cdot, \cdot \rangle_{\mathcal{H}}$:

$$\langle \mathbf{f}, \mathbf{g} \rangle_{\mathcal{H}} = \int_0^1 f^{(1)}(t)g^{(1)}(t)dt + \int_0^1 f^{(2)}(t)g^{(2)}(t)dt, \quad \mathbf{f}, \mathbf{g} \in \mathcal{H}.$$

The first step in analyzing a dataset of planar curves is to align the data, meaning to extract the shape $\tilde{\mathbf{X}}$ from \mathbf{X} or, equivalently, to identify the deformation variables in model (1). We formulate the following hypothesis regarding these deformation variables:

- ρ is a positive random scalar variable;
- $\mathbf{T} = (T_1, T_2)^\top$ is a random vector of dimension 2;
- The rotation matrix

$$\mathbf{O} = \mathbf{O}_\theta = \begin{pmatrix} \cos(\theta) & -\sin(\theta) \\ \sin(\theta) & \cos(\theta) \end{pmatrix}$$

depends on a random angle θ in $[0, 2\pi]$. Note that the case of the reflection matrix \mathbf{R}_θ can be considered using the propriety:

$$\mathbf{R}_\theta = \mathbf{O}_\theta \begin{pmatrix} 1 & 0 \\ 0 & -1 \end{pmatrix}.$$

This reduces to analyzing $(X^{(1)}, -X^{(2)})^\top$ in our framework instead of $\mathbf{X} = (X^{(1)}, X^{(2)})^\top$.

- The reparametrization function γ takes values in Γ , where Γ is defined as in (2).
- The random function $\tilde{\mathbf{X}}$ takes values in $\mathbf{S}^\infty = \{\mathbf{f} \in \mathcal{H}, \|\mathbf{f}\|_{\mathcal{H}} = 1\}$, where $\|\cdot\|_{\mathcal{H}}$ is the norm induced by $\langle \cdot, \cdot \rangle_{\mathcal{H}}$. For identification purposes, we will also assume that $\tilde{\mathbf{X}} = (\tilde{X}^{(1)}, \tilde{X}^{(2)})^\top$ is centered, i.e.

$$\int_0^1 \tilde{X}^{(1)}(t)dt = \int_0^1 \tilde{X}^{(2)}(t)dt = 0.$$

Before presenting our alignment method, we first provide the intuition behind the definition of the function space Γ .

2.1 The space of reparametrization functions Γ

Recall that we define the space of reparametrization functions as

$$\Gamma = \{\gamma_\delta(t) = \text{mod}(t - \delta, 1), t \in [0, 1], \delta \in [0, 1]\},$$

where we recall that $\text{mod}(x, 1) = x - \lfloor x \rfloor, \forall x \in \mathbb{R}$. Functions that belong to this space can be seen as a generalization of the well-known time-shift deformation warping functions for univariate functional data (see e.g. Marron et al. (2015) for details) to the case of planar closed curves. The modulo function allows to consider the cyclic nature of \mathbf{X} .

Remark. *In some context, it might be of interest to consider more flexible reparametrization functions. For example, when \mathbf{X} is related to handwritten data, "acceleration" changes must be taken into account. This can be done by modifying Γ as follows:*

$$\tilde{\Gamma} = \{\text{mod}(\gamma(t) - \delta, 1), t \in [0, 1], \delta \in [0, 1] \text{ and } \gamma \in \Gamma_0\},$$

where Γ_0 is the space of diffeomorphism functions from $[0, 1] \rightarrow [0, 1]$. Hence, this framework can be seen as an extension of the work of Tucker et al. (2013) for closed random curves.

Figure 3 exhibits the effect of $\gamma_\delta \in \Gamma$ for different values of δ on a realization $\tilde{\mathbf{x}}$ of $\tilde{\mathbf{X}}$. We see the "rearrangement effect" of the reparametrization function: $\delta = 0$ defines the reference shape and the starting point of the coordinate functions of $\tilde{\mathbf{x}} \circ \gamma_\delta$ coincides with the point $t = \delta$ of the reference shape.

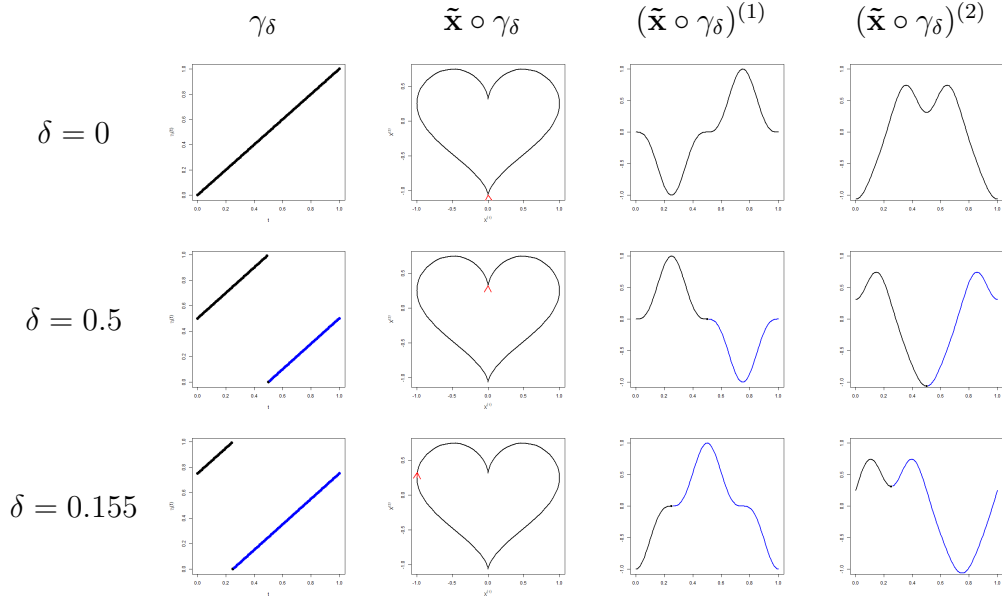


Figure 3: Plots of the functions γ_δ and of its composition with the shape $\tilde{\mathbf{x}}$ for different values of δ , resulting in different starting points (represented by the red arrows) and coordinate functions.

In contour datasets, the variation of δ arises from edge detection algorithms, which select the starting point as the argument of the coordinate functions associated with the smallest/largest distance from the origin. The issue with this approach is that the starting value depends on the transformation variables, particularly rotation. Figure 4 illustrates this effect when the smallest distance from the origin is considered: each row shows the same shape subjected to different rotations, leading to entirely different coordinate functions. Therefore, the challenge is to obtain δ jointly with the other transformation variables. We will elaborate on this point in Section 2.3.

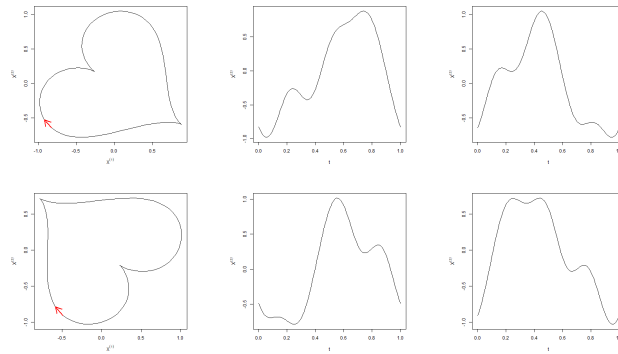


Figure 4: Illustration of the effect of rotation on a given shape and its coordinate functions when the starting value is defined as the point associated with the lowest values of the coordinate functions.

In addition to being well-suited for contour data, the space Γ has interesting mathematical properties, as demonstrated by the following result.

Proposition 2.1. (Γ, \circ) is a group and the isometry property $\|\mathbf{f} \circ \gamma_\delta\|_{\mathcal{H}} = \|\mathbf{f}\|_{\mathcal{H}}$ holds for $\mathbf{f} \in \mathcal{H}$ and $\gamma_\delta \in \Gamma$.

With this in mind, the rest of this section presents the process of determining the deformation variables $(\rho, \mathbf{O}_\theta, \mathbf{T}, \gamma_\delta)$.

2.2 Determination of the deformation variables

Although our ultimate goal is to analyze a sample of planar closed curves—that is, to work with n realizations of the random function \mathbf{X} —the alignment procedure is performed curve by curve. Specifically, for each curve, the translation and scaling variables can be directly determined based on the assumptions made about the shape $\tilde{\mathbf{X}}$, as will be discussed in Section 2.2.1. To estimate the rotation and reparametrization variables, we will see in Section 2.2.2 that it is necessary to define a template, which may depend on other curves in the sample. However, once the template is established, the alignment procedure can be applied individually to each curve.

2.2.1 The translation and scaling transformations

To determine the translation and scaling variables, we rely on the definition of the shape variable $\tilde{\mathbf{X}}$ which is centered in $(0, 0)^\top$ and has a unitary norm. Hence, direct computations show that the translation vector \mathbf{T} and the scaling parameter ρ are

$$\mathbf{T} = \int_0^1 \mathbf{X}(t) dt \quad \text{and} \quad \rho = \|\mathbf{X} - \mathbf{T}\|_{\mathcal{H}}.$$

These variables are particularly useful for analyzing an object’s position within an image : the parameter \mathbf{T} captures lateral displacement, while ρ indicates the object’s proximity to the camera.

Let \mathbf{X}^* be the variable obtained once the effect of translation and scaling has been removed from \mathbf{X} :

$$\mathbf{X}^*(t) = \frac{1}{\rho} (\mathbf{X}(t) - \mathbf{T}), \quad t \in [0, 1]. \quad (3)$$

We use this variable to determine \mathbf{O}_θ and γ_δ in the next section.

Remark. By construction, \mathbf{X}^* belongs to the same space as $\tilde{\mathbf{X}}$, namely \mathbf{S}^∞ . In statistical shape analysis, \mathbf{S}^∞ is called the “pre-shape space” (Dryden and Mardia (1998), Srivastava et al. (2010)) and it contains shapes that are possibly deformed by rotation and reparametrization. The “shape space”, which could be denoted by \mathbf{S}^∞ / \sim , represents the quotient space of \mathbf{S}^∞ with the equivalence relation \sim defined as

$$\mathbf{f} \sim \mathbf{g} \iff \exists (\theta, \gamma) \in [0, 2\pi] \times \Gamma \text{ such that } \mathbf{f} = \mathbf{O}_\theta \mathbf{g} \circ \gamma, \quad (4)$$

where $\mathbf{f}, \mathbf{g} \in \mathbf{S}^\infty$. In other words, this relation says that $\mathbf{f} \sim \mathbf{g}$ if and only if \mathbf{f} and \mathbf{g} share the same shape.

2.2.2 The rotation and reparametrization transformations

Our strategy to determine the rotation and reparametrization parameters is to align the function \mathbf{X}^* to a function of reference $\boldsymbol{\mu} \in \mathbf{S}^\infty$. As in the case of univariate functions alignment, there is no ground truth for the choice of $\boldsymbol{\mu}$ (Marron et al., 2015). It could be known a priori or estimated from the data, for example as the standardized mean of the shape

$$\boldsymbol{\mu} \propto \mathbb{E}(\tilde{\mathbf{X}}).$$

In Tucker et al. (2013), the authors propose an iterative-based Karcher's mean algorithm to approximate $\mathbb{E}(\tilde{\mathbf{X}})$ in the univariate case since direct computation of $\boldsymbol{\mu}$ is unfeasible ($\boldsymbol{\mu}$ is needed first to get $\tilde{\mathbf{X}}$). This could be extended to our case. Another strategy is to choose $\boldsymbol{\mu}$ as one of the realizations of \mathbf{X}^* . This strategy has the advantage of being faster but may inherently suffer from biases and generalization issues. The choice between these two strategies primarily depends on practical considerations. For the following theoretical developments, we assume that $\boldsymbol{\mu}$ is known. In practice, as illustrated in Sections 4 and 5, we simply select $\boldsymbol{\mu}$ as a standardized version of one of the curves from the sample.

Recall that $\mathbf{X} = \rho \mathbf{O}_\theta \tilde{\mathbf{X}} \circ \gamma_\delta + \mathbf{T}$, thus \mathbf{X}^* defined in (3) can be written as

$$\mathbf{X}^*(t) = \mathbf{O}_\theta \tilde{\mathbf{X}} \circ \gamma_\delta(t), \quad t \in [0, 1]. \quad (5)$$

Determining the rotation matrix \mathbf{O}_θ and the reparametrization function γ_δ that align \mathbf{X}^* to $\boldsymbol{\mu}$ is equivalent to finding the parameters θ and δ that minimize the distance, measured in terms of the $\|\cdot\|_{\mathcal{H}}$ norm, between $\mathbf{X}^* = \mathbf{O}_\theta \tilde{\mathbf{X}} \circ \gamma_\delta$ and $\mathbf{O}_\theta \boldsymbol{\mu} \circ \gamma_\delta$. This leads to the following definition of the parameter estimators :

$$(\hat{\theta}, \hat{\delta}) = \arg \min_{(\theta, \delta) \in [0, 2\pi] \times [0, 1]} \|\mathbf{X}^* - \mathbf{O}_\theta \boldsymbol{\mu} \circ \gamma_\delta\|_{\mathcal{H}}^2. \quad (6)$$

Using the fact that $\mathbf{O}_\theta^{-1} = \mathbf{O}_\theta^\top$, since rotation matrices are orthogonal, and that the inverse of $\gamma_\delta \in \Gamma$ is $\gamma_{1-\delta}$ (as shown in the proof of Proposition 2.1), we can estimate the shape variable $\tilde{\mathbf{X}}$, once $(\hat{\theta}, \hat{\delta})$ have been obtained, by $\mathbf{O}_{\hat{\theta}}^\top \mathbf{X}^* \circ \hat{\gamma}_{1-\hat{\delta}}$.

From the isometry propriety of Γ (Proposition 2.1), it follows that

$$\|\mathbf{f} \circ \gamma - \mathbf{g} \circ \gamma\|_{\mathcal{H}} = \|\mathbf{f} - \mathbf{g}\|_{\mathcal{H}}, \quad \text{for } \mathbf{f}, \mathbf{g} \in \mathcal{H} \text{ and } \gamma \in \Gamma.$$

As in the univariate case (Tucker et al., 2013), this invariance ensures that our estimators remain unchanged under an identical reparametrization of \mathbf{X}^* and $\boldsymbol{\mu}$.

Remark. Equation (6) and Proposition 2.1 enable the introduction of the following "elastic distance" $d : \mathbf{S}^\infty \times \mathbf{S}^\infty \rightarrow \mathbb{R}^+$, inspired by Younes (1998) and Srivastava and Klassen (2016):

$$d(\mathbf{f}, \mathbf{g}) = \min_{\delta \in [0, 1], \theta \in [0, 2\pi]} \|\mathbf{f} \circ \gamma_\delta - \mathbf{O}_\theta \mathbf{g}\|_{\mathcal{H}}.$$

It is "elastic" since by construction $d(\cdot, \cdot)$ is independent of rotation and reparametrization:

$$d(\mathbf{f}, \mathbf{g}) = d(\mathbf{O}_{\theta_1} \mathbf{f} \circ \gamma_{\delta_1}, \mathbf{O}_{\theta_2} \mathbf{g} \circ \gamma_{\delta_2})$$

for δ_1, δ_2 in $[0, 1]$ and $\theta_1, \theta_2 \in [0, 2\pi]$. This means that $d(\mathbf{X}^*, \tilde{\mathbf{X}}) = 0$. In fact, we can use $d(\cdot, \cdot)$ to reformulate the equivalence relation in (4) as follows:

$$\mathbf{f} \sim \mathbf{g} \iff d(\mathbf{f}, \mathbf{g}) = 0,$$

where $\mathbf{f}, \mathbf{g} \in \mathbf{S}^\infty$. The equivalence class $[\mathbf{f}]$ of \mathbf{f} is

$$[\mathbf{f}] = \{\mathbf{g} \in \mathcal{H}, d(\mathbf{f}, \mathbf{g}) = 0\}.$$

The set $[\mathbf{f}]$ is also called the "orbit" of \mathbf{f} (Srivastava and Klassen, 2016).

Lemma 2.2. $d(\cdot, \cdot)$ is a pseudo-distance on \mathcal{H} .

Note that $d(\cdot, \cdot)$ is not a proper distance since separability does not hold, indeed

$$d(\mathbf{f}, \mathbf{g}) = 0 \not\Rightarrow \mathbf{f} = \mathbf{g},$$

but by redefining it on the shape space \mathbf{S}^∞ / \sim instead of the pre-shape \mathbf{S}^∞ , it can be made into one.

2.3 Estimation of deformations using a basis expansion for \mathbf{X}

Due to technological limitations, functional variables can only be observed discretely in practice. In our case, the discretization grid coincides with the image resolution. Therefore, a crucial first step in FDA is data smoothing, which consists of reconstructing the functional form of each discretely observed curve. Working with the continuous version of the data instead of analyzing images at the pixel level is a major advantage of our approach, as it enables the handling of images with different resolutions.

A common method for data smoothing is to use a basis function system (Ramsey and Silverman, 2005, Chap. 3). This approach is particularly suitable in our context, as it allows us to express the deformations estimation problem in a linear matrix formulation, making it more computationally tractable than working directly in the functional space.

The basis expansion technique assumes that \mathbf{X} can be expressed as

$$\mathbf{X}(t) = \sum_{k=0}^M \mathbf{c}_k \psi_k(t), \quad t \in [0, 1],$$

where $\psi_0, \dots, \psi_M \in L^2([0, 1])$ are known basis functions, and $\mathbf{c}_k \in \mathbb{R}^2$ are the corresponding coefficients. Reconstructing the full function \mathbf{X} from discrete observations thus reduces to estimating the coefficients \mathbf{c}_k , which can be achieved, for instance, by minimizing a least-squares criterion.

The choice of basis functions ψ_k depends on the context. In FDA, B-splines and Fourier basis functions are among the most commonly used options: B-splines are typically preferred for non-periodic data, while Fourier basis functions are well suited for periodic data (Ramsey and Silverman, 2005).

In this work, we focus on Fourier basis functions due to the inherent periodicity of \mathbf{X} . A key benefit of this choice is the well-known "time shift" property of the Fourier transform, which, as we will show, greatly simplifies the optimization problem (6).

First recall that the first $M + 1$ Fourier basis functions are

$$\psi_0(t) = 1, \quad \psi_k(t) = \begin{cases} \sqrt{2} \sin((k+1)\pi t) & \text{if } k \text{ odd,} \\ \sqrt{2} \cos(k\pi t) & \text{if } k \text{ even,} \end{cases} \quad (7)$$

for $k = 1, \dots, M$ and M even. Since these functions are orthonormal and satisfy $\int_0^1 \psi_k(t) dt = 0, k \geq 1$, the translation and scaling parameters can be written as

$$\mathbf{T} = \int_0^1 \mathbf{X}(t) dt = \mathbf{c}_0 \text{ and } \rho = \|\mathbf{X} - \mathbf{T}\|_{\mathcal{H}} = \left\| \sum_{k=1}^M \mathbf{c}_k \psi_k \right\|_{\mathcal{H}} = \sqrt{\sum_{k=1}^M \|\mathbf{c}_k\|_2^2}, \quad (8)$$

with $\|\cdot\|_2$ the ℓ^2 -vector norm. This leads to

$$\mathbf{X}^*(t) = \frac{1}{\rho} (\mathbf{X}(t) - \mathbf{T}) = \sum_{k=1}^M \boldsymbol{\alpha}_k \psi_k(t) = \boldsymbol{\alpha} \boldsymbol{\psi}(t),$$

with $\boldsymbol{\alpha}_k = \mathbf{c}_k / \rho \in \mathbb{R}^2, k = 1, \dots, M$, and where $\boldsymbol{\alpha} = (\boldsymbol{\alpha}_1, \boldsymbol{\alpha}_2, \dots, \boldsymbol{\alpha}_M) \in \mathbb{R}^{2 \times M}$ and $\boldsymbol{\psi} = (\psi_1, \psi_2, \dots, \psi_M)^\top \in (L^2([0, 1]))^M$.

The next lemma formalizes the "time shift" property by describing how reparametrization affects Fourier basis functions.

Lemma 2.3. *Let ψ_1, \dots, ψ_M be defined as in (7) and define $\boldsymbol{\psi}_\delta = (\psi_1 \circ \gamma_\delta, \dots, \psi_M \circ \gamma_\delta)^\top$, with $\gamma_\delta \in \Gamma$. Then we have*

$$\boldsymbol{\psi} = \boldsymbol{\beta}(\delta) \boldsymbol{\psi}_\delta, \quad (9)$$

where

$$\boldsymbol{\beta}(\delta) = \begin{pmatrix} \mathbf{O}_{2\pi\delta} & \mathbf{0} & \dots & \mathbf{0} \\ \mathbf{0} & \mathbf{O}_{4\pi\delta} & \dots & \mathbf{0} \\ \vdots & \vdots & \dots & \vdots \\ \mathbf{0} & \mathbf{0} & \dots & \mathbf{O}_{M\pi\delta} \end{pmatrix} \in \mathbb{R}^{M \times M},$$

is a sparse-orthogonal matrix.

This result reduces the reparametrization to a simple linear change of basis functions, where $\boldsymbol{\beta}(\delta)$ is the transfer matrix. Note that if $\delta \in \{0, 1\}$, the matrix $\boldsymbol{\beta}(\delta)$ corresponds to the identity matrix, meaning that the reparametrization effect vanishes. The next result builds on this lemma to reformulate the objective function in (6), allowing it to be expressed in a matrix form rather than a functional form.

Proposition 2.4. *Suppose that the function of reference $\boldsymbol{\mu}$ can be expressed as*

$$\boldsymbol{\mu}(t) = \sum_{k=1}^M \mathbf{u}_k \psi_k(t) = \mathbf{u} \boldsymbol{\psi}(t),$$

with $\mathbf{u} = (\mathbf{u}_1, \mathbf{u}_2, \dots, \mathbf{u}_M) \in \mathbb{R}^{2 \times M}$. Then the optimization problem (6) is equivalent to

$$(\hat{\theta}, \hat{\delta}) = \arg \min_{(\theta, \delta) \in [0, 2\pi] \times [0, 1]} \|\boldsymbol{\alpha} \boldsymbol{\beta}(\delta) - \mathbf{O}_\theta \mathbf{u}\|_F^2 \quad (10)$$

where $\|\cdot\|_F$ is the Frobenius norm matrix.

The problem (10) is a variation of the Procrustes problem (Schönemann, 1966). In the classical formulation, the goal is to determine the angle θ , whereas in our case, we also need to estimate δ .

To achieve this, we first construct a candidate set \mathcal{S} for $\hat{\delta}$. For each $\hat{\delta} \in \mathcal{S}$, the corresponding $\hat{\theta}$ is obtained directly as the Procrustes angle solution. This results in multiple candidate pairs $(\hat{\delta}, \hat{\theta})$, and we select the one yielding the minimal value of the objective function $\mathcal{F}(\theta, \delta) = \|\boldsymbol{\alpha}\boldsymbol{\beta}(\delta) - \mathbf{O}_\theta\mathbf{u}\|_F^2$.

One strategy for defining \mathcal{S} is as follows. First minimize the function $\mathcal{F}(\theta, \delta)$ with respect to δ , and let \mathcal{S}_0 denote the set of solutions. Then define \mathcal{S} as \mathcal{S}_0 . The set \mathcal{S}_0 can be computed in the following way. Direct calculations lead to

$$\begin{aligned} \mathcal{F}(\theta, \delta) = & \|\boldsymbol{\alpha}\|_F^2 + \|\mathbf{u}\|_F^2 - 2\cos(\theta) [\boldsymbol{\alpha}^{(1)}\boldsymbol{\beta}(\delta)(\mathbf{u}^{(1)})^\top + \boldsymbol{\alpha}^{(2)}\boldsymbol{\beta}(\delta)(\mathbf{u}^{(2)})^\top] \\ & + 2\sin(\theta) [\boldsymbol{\alpha}^{(1)}\boldsymbol{\beta}(\delta)(\mathbf{u}^{(2)})^\top - \boldsymbol{\alpha}^{(2)}\boldsymbol{\beta}(\delta)(\mathbf{u}^{(1)})^\top]. \end{aligned}$$

The partial derivatives of \mathcal{F} are given by:

$$\begin{aligned} \frac{\partial}{\partial\theta}\mathcal{F}(\theta, \delta) = & -2\cos(\theta) [\boldsymbol{\alpha}^{(2)}\boldsymbol{\beta}(\delta)(\mathbf{u}^{(1)})^\top - \boldsymbol{\alpha}^{(1)}\boldsymbol{\beta}(\delta)(\mathbf{u}^{(2)})^\top] \\ & + 2\sin(\theta) [\boldsymbol{\alpha}^{(1)}\boldsymbol{\beta}(\delta)(\mathbf{u}^{(1)})^\top + \boldsymbol{\alpha}^{(2)}\boldsymbol{\beta}(\delta)(\mathbf{u}^{(2)})^\top], \\ \frac{\partial}{\partial\delta}\mathcal{F}(\theta, \delta) = & -2\cos(\theta) [\boldsymbol{\alpha}^{(1)}\mathbf{G}(\delta)(\mathbf{u}^{(1)})^\top + \boldsymbol{\alpha}^{(2)}\mathbf{G}(\delta)(\mathbf{u}^{(2)})^\top] \\ & + 2\sin(\theta) [\boldsymbol{\alpha}^{(1)}\mathbf{G}(\delta)(\mathbf{u}^{(2)})^\top - \boldsymbol{\alpha}^{(2)}\mathbf{G}(\delta)(\mathbf{u}^{(1)})^\top]. \end{aligned}$$

Using the fact that the optimums verify

$$\frac{\partial}{\partial\delta}\mathcal{F}(\theta, \delta) = \frac{\partial}{\partial\theta}\mathcal{F}(\theta, \delta) = 0,$$

we have that

$$\mathcal{S}_0 = \left\{ \delta \in [0, 1], \frac{\boldsymbol{\alpha}^{(2)}\boldsymbol{\beta}(\delta)(\mathbf{u}^{(1)})^\top - \boldsymbol{\alpha}^{(1)}\boldsymbol{\beta}(\delta)(\mathbf{u}^{(2)})^\top}{\boldsymbol{\alpha}^{(1)}\boldsymbol{\beta}(\delta)(\mathbf{u}^{(1)})^\top + \boldsymbol{\alpha}^{(2)}\boldsymbol{\beta}(\delta)(\mathbf{u}^{(2)})^\top} = \frac{\boldsymbol{\alpha}^{(1)}\mathbf{G}(\delta)(\mathbf{u}^{(1)})^\top + \boldsymbol{\alpha}^{(2)}\mathbf{G}(\delta)(\mathbf{u}^{(2)})^\top}{\boldsymbol{\alpha}^{(1)}\mathbf{G}(\delta)(\mathbf{u}^{(2)})^\top - \boldsymbol{\alpha}^{(2)}\mathbf{G}(\delta)(\mathbf{u}^{(1)})^\top} \right\},$$

where $\mathbf{G}(\delta) = \frac{\partial}{\partial\delta}\boldsymbol{\beta}(\delta)$.

However, \mathcal{S}_0 has no closed-form expression. A possible workaround is to approximate it by the set of solutions of the following equation:

$$\left\| \frac{\boldsymbol{\alpha}^{(2)}\boldsymbol{\beta}(\delta)(\mathbf{u}^{(1)})^\top - \boldsymbol{\alpha}^{(1)}\boldsymbol{\beta}(\delta)(\mathbf{u}^{(2)})^\top}{\boldsymbol{\alpha}^{(1)}\boldsymbol{\beta}(\delta)(\mathbf{u}^{(1)})^\top + \boldsymbol{\alpha}^{(2)}\boldsymbol{\beta}(\delta)(\mathbf{u}^{(2)})^\top} - \frac{\boldsymbol{\alpha}^{(1)}\mathbf{G}(\delta)(\mathbf{u}^{(1)})^\top + \boldsymbol{\alpha}^{(2)}\mathbf{G}(\delta)(\mathbf{u}^{(2)})^\top}{\boldsymbol{\alpha}^{(1)}\mathbf{G}(\delta)(\mathbf{u}^{(2)})^\top - \boldsymbol{\alpha}^{(2)}\mathbf{G}(\delta)(\mathbf{u}^{(1)})^\top} \right\|_2 = 0,$$

which can be solved numerically. While feasible, this approach has a significant drawback: any approximation error in \mathcal{S}_0 may lead to inaccurate estimates of (θ, δ) , potentially degrading the overall alignment accuracy.

Based on some numerical experiments, we propose a much simpler alternative: instead of computing \mathcal{S}_0 , we define \mathcal{S} as a dense grid over $[0, 1]$. This strategy, which we adopt in our simulation study, gives good estimates of the parameters δ and θ , as will be discussed in Section 4.

3 Modeling \mathbf{X} : a joint PCA approach

In the previous section, we introduced tools for estimating the deformation parameters associated with a planar curve \mathbf{X} . This enables us to align a sample of planar closed curves by removing these deformations curve-by-curve, allowing for a meaningful analysis of variations in both shape and deformation variables.

In this section, we define a statistical model to capture the full range of variations in \mathbf{X} , a key challenge in many applications dealing with such data. A straightforward approach might be to use a linear model for \mathbf{X} , but this is unsuitable due to the nonlinear nature of deformations acting on $\tilde{\mathbf{X}}$. This is evident when considering the expectation of \mathbf{X} :

$$\mathbb{E}(\mathbf{X}) = \mathbb{E} \left(\rho \mathbf{O}_\theta \left(\tilde{\mathbf{X}} \circ \gamma_\delta \right) \right) + \mathbb{E}(\mathbf{T}).$$

Here, the deformations are entangled within the term $\mathbb{E} \left(\rho \mathbf{O}_\theta \left(\tilde{\mathbf{X}} \circ \gamma_\delta \right) \right)$, making it difficult to identify and analyze their individual contributions.

To tackle this problem, and inspired by the phase-amplitude joint modeling in Tucker et al. (2013), we propose to study the random vector $\mathbf{Z} = (\mathbf{Z}_1, \mathbf{Z}_2)^\top$ of mixed variables:

$$\mathbf{Z}_1 = \rho \tilde{\mathbf{X}} \in \mathcal{H} \quad \text{and} \quad \mathbf{Z}_2^\top = \left(\tan\left(\frac{\pi}{2}(\delta - \frac{1}{2})\right) \quad \tan\left(\frac{1}{4}(\frac{1}{2}\theta - \pi)\right) \quad \mathbf{T}^\top \right) \in \mathbb{R}^4.$$

The variable $\mathbf{Z}_1 \in \mathcal{H}$ is a linear transformation of the vector $(\tilde{\mathbf{X}}, \rho) \in \mathbf{S}^\infty \times \mathbb{R}^+$ preserving the same information. However, working with \mathbf{Z}_1 is more convenient, as the space \mathbf{S}^∞ is inherently restrictive : it does not naturally support meaningful definitions of functional expectations or covariance operators. Nevertheless, if ρ is considered as a nuisance parameter and discarded, one can analyze $\tilde{\mathbf{X}}$ through a tangent space transformation, providing an alternative framework for shape analysis (see Dryden and Mardia (1998) and Tucker et al. (2013) for more details). Similarly, we work with the variable $\mathbf{Z}_2 \in \mathbb{R}^4$ instead of $(\delta, \theta, \mathbf{T}^\top)^\top \in [0, 1] \times [0, 2\pi] \times \mathbb{R}^2$, as \mathbf{Z}_2 is defined in a more convenient space.

In summary, \mathbf{Z} is obtained via the bijective transformation

$$\mathcal{G}_1 : \mathcal{H} \rightarrow \mathcal{H} \times \mathbb{R}^4,$$

defined such that $\mathcal{G}_1(\mathbf{X}) = \mathbf{Z}$. Moreover, letting $\mathbf{Z}_2^\top = (Z_{21}, Z_{22}, Z_{23}, Z_{24})$ we can recover \mathbf{X} from \mathbf{Z} using

$$\mathbf{X} = \mathcal{G}_1^{-1}(\mathbf{Z}) = \mathbf{O}_{8 \tan^{-1}(Z_{22}) + 2\pi} \mathbf{Z}_1 \circ \gamma_{\frac{2}{\pi} \tan^{-1}(Z_{21}) + \frac{1}{\pi}}(t) + (Z_{23}, Z_{24})^\top.$$

3.1 The underlying linear models

Having properly defined \mathbf{Z} , we now aim to model its two components independently using PCA-based techniques.

Since \mathbf{Z}_1 is a bivariate functional variable, we use the Multivariate Functional PCA (MFPCA) approach of Jacques and Preda (2014) which leads to

$$\mathbf{Z}_1(t) = \mathbb{E}(\mathbf{Z}_1(t)) + \sum_{k=1}^{M_1} \xi_k^{(1)} \phi_k(t), \quad t \in [0, 1], \quad (11)$$

where $\phi_1, \phi_2, \dots, \phi_{M_1} \in \mathcal{H}$ are the eigenfunctions of the covariance operator of \mathbf{Z}_1 . Similarly, classical PCA gives the following representation of \mathbf{Z}_2 :

$$\mathbf{Z}_2 = \mathbb{E}(\mathbf{Z}_2) + \sum_{k=1}^{M_2} \xi_k^{(2)} \mathbf{U}_k, \quad (12)$$

where $\mathbf{U}_1, \mathbf{U}_2, \dots, \mathbf{U}_{M_2} \in \mathbb{R}^4$ are the eigenvectors of the covariance matrix of \mathbf{Z}_2 . For $j = 1, 2$, we have that the scores $\xi_1^{(j)}, \dots, \xi_{M_j}^{(j)} \in \mathbb{R}$ are mean-zero random variables such that

$$\mathbb{E}(\xi_k^{(j)} \xi_l^{(j)}) = \begin{cases} \lambda_k^{(j)} & \text{if } k = l, \\ 0 & \text{if } k \neq l, \end{cases}$$

where $\lambda_k^{(j)}$ is the k -th eigenvalue of the covariance operator of \mathbf{Z}_j .

It is worth noting that a global PCA approach could be applied to \mathbf{Z} , treating both components simultaneously. This could be achieved using, for example, techniques designed for hybrid variables (as developed in Chap.10 of Ramsey and Silverman (2005)). However, while this approach may simplify the representation, it comes at the cost of interpretability. Indeed, in this case, the scores for shape and deformation would no longer be separated. As a result, if a curve exhibits an abnormal score, it would be unclear whether this deviation is due to shape or deformation variations.

By contrast, our separated PCA approach provides greater transparency by disentangling shape and deformation variations. This interpretability is particularly valuable in applications such as anomaly detection and classification, where understanding the source of variations can be important.

3.2 The generative model of \mathbf{X}

The scores in (11) and (12) can be modeled using the same techniques as used in the univariate functional case (Tucker, 2023). For example, a classical approach would be to use a joint Gaussian model which supposes that the random vector of scores

$$\boldsymbol{\xi}^\top = ((\boldsymbol{\xi}^{(1)})^\top, (\boldsymbol{\xi}^{(2)})^\top) = (\xi_1^{(1)}, \dots, \xi_{M_1}^{(1)}, \xi_1^{(2)}, \dots, \xi_{M_2}^{(2)}) \in \mathbb{R}^{M_1+M_2}$$

follows a multivariate normal distribution of mean $\mathbf{0} \in \mathbb{R}^{M_1+M_2}$ and of covariance

$$\boldsymbol{\Sigma} = \begin{pmatrix} \boldsymbol{\Sigma}_1 & \boldsymbol{\Sigma}_{1,2} \\ \boldsymbol{\Sigma}_{1,2}^\top & \boldsymbol{\Sigma}_2 \end{pmatrix} \in \mathbb{R}^{(M_1+M_2) \times (M_1+M_2)}$$

where

$$\boldsymbol{\Sigma}_{1,2} = \mathbb{E}(\boldsymbol{\xi}^{(1)}(\boldsymbol{\xi}^{(2)})^\top) \in \mathbb{R}^{(M_1 \times M_2)} \quad \text{and} \quad \boldsymbol{\Sigma}_j = \begin{pmatrix} \lambda_1^{(j)} & 0 & \dots & 0 \\ 0 & \lambda_2^{(j)} & \dots & 0 \\ \vdots & & \dots & \\ 0 & 0 & \dots & \lambda_{M_j}^{(j)} \end{pmatrix} \in \mathbb{R}^{M_j \times M_j}, j = 1, 2.$$

Once a model has been specified for $\boldsymbol{\xi}$, it is straightforward to define a generative model for \mathbf{X} . Define the operator \mathcal{G}_2 as the bijective transformation of \mathbf{Z} into $\boldsymbol{\xi}$ obtained by the joint-PCA approach, i.e.,

$$\mathcal{G}_2 : \mathcal{H} \times \mathbb{R}^4 \rightarrow \mathbb{R}^{M_1+M_2}$$

such that $\mathcal{G}_2(\mathbf{Z}) = \boldsymbol{\xi}$. Then, the generative model of \mathbf{X} is

$$\mathbf{X} = \mathcal{G}_1^{-1}(\mathbf{Z}) = \mathcal{G}_1^{-1}(\mathcal{G}_2^{-1}(\boldsymbol{\xi})). \quad (13)$$

4 Simulation study

In order to study the performance of the estimation procedure presented in the previous sections, we consider two main scenarios :

S1 we observe realizations $\mathbf{X}_1^*, \dots, \mathbf{X}_n^*$ of \mathbf{X}^* , on a common discrete grid ;

S2 we observe realizations $\mathbf{X}_1, \dots, \mathbf{X}_n$ of \mathbf{X} , on a common discrete grid.

Scenario **S1** allows us to focus exclusively on the estimation of the rotation matrix and the reparametrization function, as they are the core elements of our estimation procedure. In contrast, scenario **S2** represents a more realistic setting by considering all deformation variables.

4.1 Data simulation

We construct the planar closed curves \mathbf{X}_i by setting

$$\mathbf{X}_i(t) = \rho_i \mathbf{X}_i^*(t) + \mathbf{T}_i, \text{ where } \mathbf{X}_i^*(t) = \mathbf{O}_{\theta_i} \tilde{\mathbf{X}}_i \circ \gamma_{\delta_i}(t), t \in [0, 1],$$

with $\mathbf{T}_i \sim N((0,0)^\top, \mathbf{I}_2)$, $\delta_i \sim U(0, 1)$, and $\theta_i \equiv 2\pi\delta_i \sim U(0, 2\pi)$. Inspired by Weisstein (2003), we define the scaled shape variables $\rho_i \tilde{\mathbf{X}}_i$ to have a "heart" shape by setting

$$\rho_i \tilde{\mathbf{X}}_i(t) = \begin{pmatrix} b_{i0} \sin^3(\pi(2t-1)) \\ \sum_{k=1}^4 b_{ik} \cos(k\pi(2t-1)) \end{pmatrix}, t \in [0, 1],$$

with $(b_{i0}, \dots, b_{i4}) \sim N((16, 13, -5, -2, -1)^\top, \sigma^2 \mathbf{I}_5)$ and we consider two different values for σ : 0.01 and 0.1. Note that since by definition we require $\tilde{\mathbf{X}}_i \in \mathbf{S}^\infty$, the parameter ρ_i is equal to $\|\rho_i \tilde{\mathbf{X}}_i\|_{\mathcal{H}}$.

A standardized version of the mean function $\mathbf{f}(t) = \mathbb{E}(\rho_i \tilde{\mathbf{X}}_i(t))$ is illustrated in the first row of Figure 5. To illustrate the effect of the parameter σ on the shape variables, the second and third rows of the figure show $n = 5$ curves, $\tilde{\mathbf{X}}_1, \dots, \tilde{\mathbf{X}}_5$, simulated under the two considered values of σ . Figure 6 shows 3 realizations of \mathbf{X}^* (first three columns) and 3 realizations of \mathbf{X} (last three columns), both simulated with $\sigma = 0.1$.

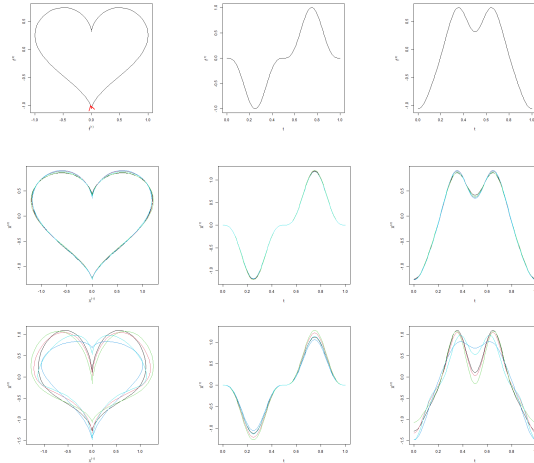


Figure 5: Plot of the function $\mathbf{f}/\|\mathbf{f}\|_{\mathcal{H}}$ and of its coordinate functions (first row), plot of $n = 5$ realizations of $\tilde{\mathbf{X}}$ and of their coordinate functions, simulated with $\sigma = 0.01$ (second row) and $\sigma = 0.1$ (third row).

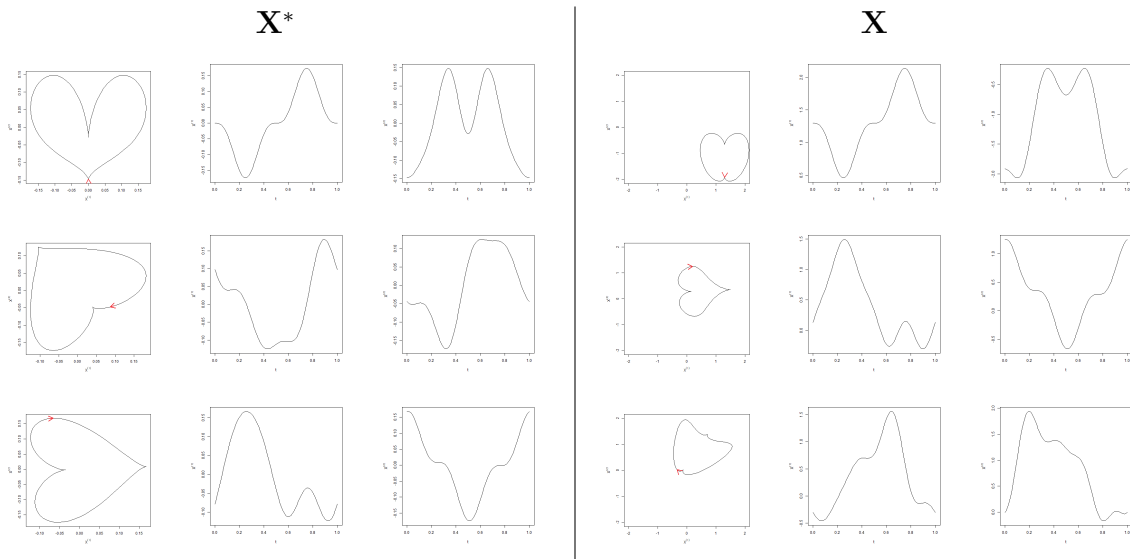


Figure 6: Plot of 3 realizations of \mathbf{X}^* and of their coordinate functions on the left and plot of 3 realizations of \mathbf{X} and of their coordinate functions on the right, obtained under $\sigma = 0.1$.

4.2 Numerical results

We simulated four samples of $n = 200$ curves, each observed on a common grid of 101 equidistant points on $[0, 1]$. Each sample corresponds to a different combination of scenarios and values of σ . We then estimated the functional form of each discretely observed curve using a basis expansion strategy, as described in Section 2.3, with $M = 10$ Fourier basis. This number of basis ensures a sufficiently good fit to the data.

The estimated curves of each sample, denoted $\hat{\mathbf{x}}_i^*$, (respectively $\hat{\mathbf{x}}_i$), $i = 1, \dots, n$ for scenario 1 (resp. for scenario 2) are illustrated in the three first columns of Figure 7.

We then applied the estimation procedure presented in Section 2, using $\boldsymbol{\mu} = \mathbf{f} / \|\mathbf{f}\|_{\mathcal{H}}$ as the function of reference and $\mathcal{S} = \{0.01k\}_{k=1}^{100}$ as the candidate set for $\hat{\delta}$. The last three columns of Figure 7 show the estimated shape curves, $\hat{\mathbf{x}}_i, i = 1, \dots, n$, for each sample. Visually, the results are satisfactory: the shape curves are similar to those depicted in Figure 5 and the coordinate functions are well aligned, meaning that their modes coincide properly.

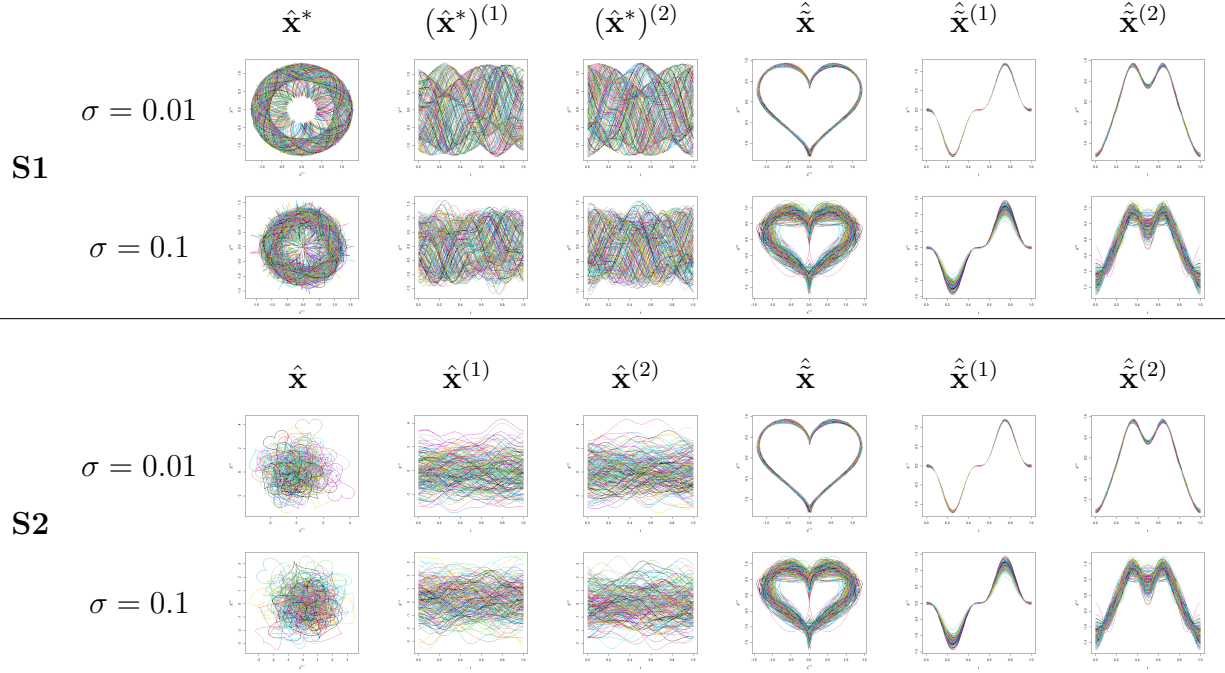


Figure 7: Each row corresponds to a sample, the first three columns show the smoothed curves and their coordinate functions while the three last show the estimations of the shape curves.

To quantitatively assess the performance of our estimation procedure, we use Mean Square Error (MSE) metrics. For the translation and scaling parameters, these are defined as :

$$\text{MSE}_{\mathbf{T}} = \frac{1}{n} \sum_{i=1}^n \left\| \mathbf{T}_i - \hat{\mathbf{T}}_i \right\|_2^2 \text{ and } \text{MSE}_{\rho} = \frac{1}{n} \sum_{i=1}^n (\rho_i - \hat{\rho}_i)^2.$$

To account for the cyclic nature of the rotation and re-parametrization parameters, i.e., the fact that values at the boundaries of their respective domain, $[0, 2\pi]$ and $[0, 1]$, are equivalent, we define the MSE on a projected version of these parameters as follows:

$$\text{MSE}_{\theta} = \frac{1}{n} \sum_{i=1}^n \left\| \begin{pmatrix} \cos(\theta_i) \\ \sin(\theta_i) \end{pmatrix} - \begin{pmatrix} \cos(\hat{\theta}_i) \\ \sin(\hat{\theta}_i) \end{pmatrix} \right\|_2^2$$

and

$$\text{MSE}_{\delta} = \frac{1}{n} \sum_{i=1}^n \left\| \begin{pmatrix} \cos(2\pi\delta_i) \\ \sin(2\pi\delta_i) \end{pmatrix} - \begin{pmatrix} \cos(2\pi\hat{\delta}_i) \\ \sin(2\pi\hat{\delta}_i) \end{pmatrix} \right\|_2^2.$$

Table 1 summarizes the results, displaying the MSE values for each parameter, scenario, and value of σ . All values in the table are very small, indicating a high accuracy of the estimated parameters.

	σ	MSE_δ	MSE_θ	MSE_T	MSE_ρ
S1	0.01	3.40×10^{-4}	3.42×10^{-4}		
	0.1	3.14×10^{-4}	3.15×10^{-4}		
S2	0.01	3.39×10^{-4}	3.41×10^{-4}	9.98×10^{-32}	1.80×10^{-32}
	0.1	3.15×10^{-4}	3.15×10^{-4}	6.34×10^{-32}	1.81×10^{-32}

Table 1: MSE of the estimated parameters for the different scenarios and values of σ

5 Real data analysis

In this section, we analyze datasets from the *MPEG-7* database¹, which has been widely used in statistical shape analysis (see, for example, Srivastava et al. (2010), Srivastava and Klassen (2016), Carlier et al. (2016)). This database contains binarized images of 101 different objects, each with approximately 20 images. For our study, we focus on five specific objects: the butterfly, the fork, the bat, the horseshoe, and the spoon. For clarity, we present in this section only the results for the butterfly and the fork datasets, while the results for the other three objects are provided in Appendix A. Figure 8 displays five sample images for each of the two objects under consideration. We see that the images exhibit variations in rotation, scaling, and translation, resulting in differences in the orientation, size, and positioning of the butterflies and forks.

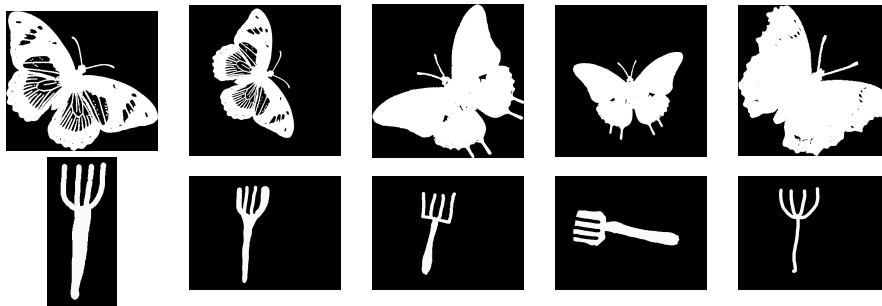


Figure 8: Examples of images from the database for the butterfly and fork objects.

Before analyzing the datasets with our approach, we first need to extract planar curves from the binarized images. To do so, we use the OpenCV library in Python (Bradski, 2000). For illustration, Figure 9 displays the planar closed curves extracted from the images in Figure 8. We can observe that the extraction procedure introduces reparametrization variations: the starting points are generally different across curves, particularly for the forks. It is also worth noting that the distribution of deformation variables appears to differ between the two objects. Indeed, for example, almost all butterflies exhibit different orientations, whereas the forks are almost all aligned in the same direction; this suggests that the distribution

¹<https://dabi.temple.edu/external/shape/MPEG7/dataset.html>

of the rotation parameter varies across objects. In a general context, this means that the deformations applied to a shape may depend on the shape itself.

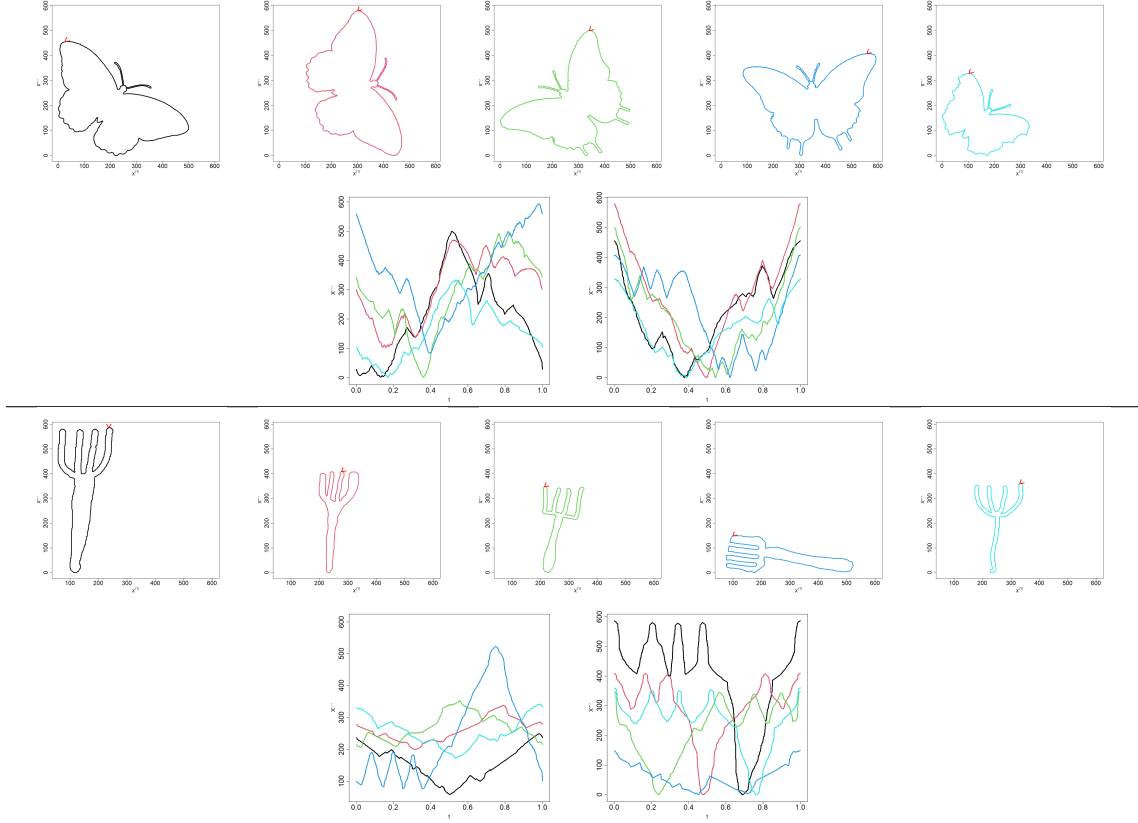


Figure 9: Planar closed curves extracted from the binarized images of Figure 8 (first row of each block) with their associate first and second coordinate functions (second row of each block).

5.1 Results from the alignment procedure

Before aligning the planar curves – that is, estimating the deformation parameters – we first recover their functional form using a basis expansion with $M = 50$ Fourier functions. Let $\hat{\mathbf{x}}_1^s, \dots, \hat{\mathbf{x}}_{n_s}^s$ denote the resulting functions, where the index s refers to the dataset: $s = b$ for butterflies and $s = f$ for forks. We then estimate the translation and scaling parameters for each curve, yielding the standardized shapes $\hat{\mathbf{x}}_i^{*s}, i = 1, \dots, n_s$. These standardized shapes are illustrated in Figure 10.

To estimate the rotation and the reparametrization parameters, we use the first estimated standardized shape associate to each dataset as the function of reference, setting $\boldsymbol{\mu}^s = \hat{\mathbf{x}}_1^{*s}$. We then define the candidate set for $\hat{\delta}$ as $\mathcal{S} = \{0.01k\}_{k=1}^{100}$. This procedure results in the estimated shape curves $\hat{\mathbf{x}}_i^s, i = 1, \dots, n_s$ which are illustrated in Figure 10. The coordinate functions are visually well aligned, indicating that the alignment procedure performs well.

The estimated deformation parameters for each curve in both datasets are shown in Figure 11. We observe differences in the distribution of these parameters across the two datasets.

For example, in the butterfly dataset, the second translation coordinate $\hat{T}_i^{(2)}$ appears to be linearly related to the first coordinate $\hat{T}_i^{(1)}$, whereas in the fork dataset, the translation vectors are mainly clustered around a centroid. Moreover, the estimated rotation parameters $\hat{\theta}_i$ exhibit greater variability in the butterfly dataset compared to the fork dataset, and this remark also holds for the reparametrization parameters. These observations confirm our visual assessment in Figure 9: the distributions of deformation variables are shape-dependent and should be accounted for in the generative model of the planar curves \mathbf{X} , as we will discuss in the next section.

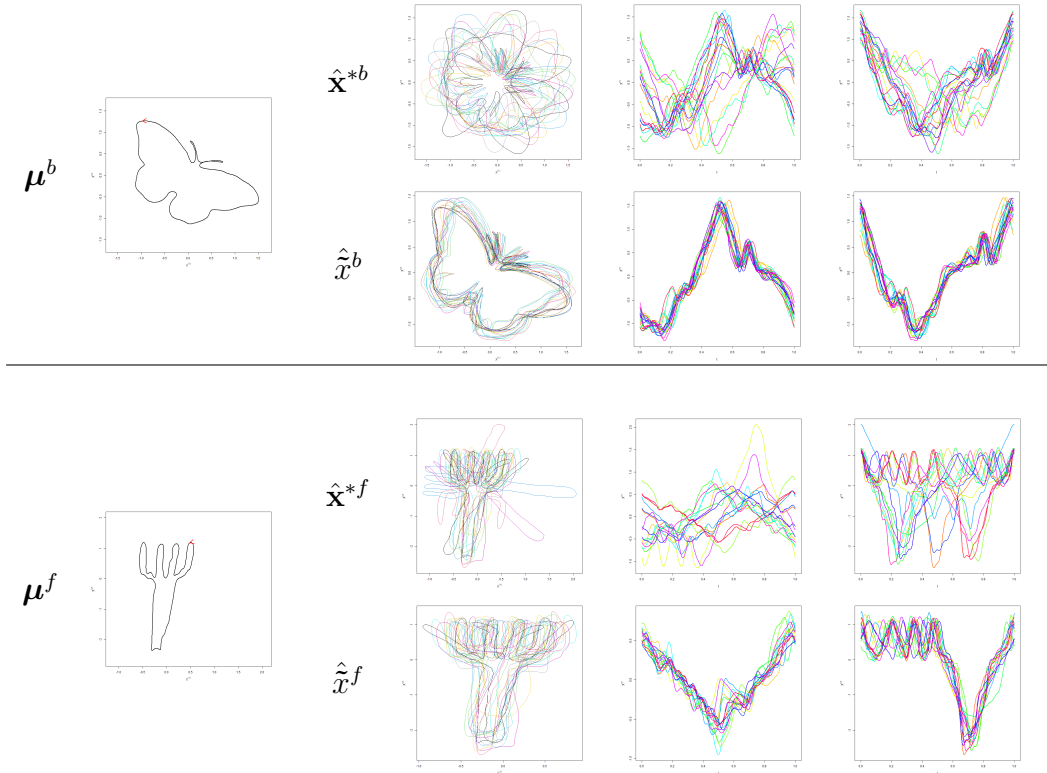


Figure 10: Illustration of the estimates of the standardized shapes (first row) and of the shapes (second) obtained from applying our alignment procedure to the butterfly (first block) and fork (second block) datasets.

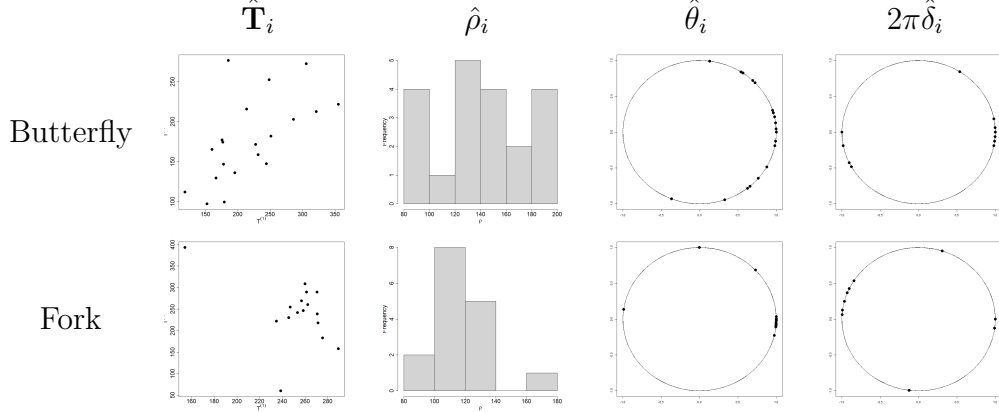


Figure 11: Plots of the estimated deformation parameters of each curve in both datasets

5.2 Results from modeling \mathbf{X}

We now apply the joint PCA methodology presented in Section 3.1 to both datasets. For each curve \mathbf{x}_i in each dataset, we construct the vector

$$\mathbf{z}_i = \mathcal{G}_1(\hat{\rho}_i \mathbf{O}_{\hat{\theta}_i} \hat{\mathbf{x}}_i \circ \gamma_{\hat{\delta}_i} + \hat{\mathbf{T}}_i) = (\mathbf{z}_{i1}, \mathbf{z}_{i2})^\top,$$

where

$$\mathbf{z}_{i1} = \hat{\rho}_i \hat{\mathbf{x}}_i \text{ and } \mathbf{z}_{i2}^\top = \left(\tan\left(\frac{\pi}{2}(\hat{\delta}_i - \frac{1}{2})\right) \quad \tan\left(\frac{1}{4}(\frac{1}{2}\hat{\theta}_i - \pi)\right) \quad \hat{\mathbf{T}}_i^\top \right)^\top.$$

We then analyze the \mathbf{z}_{i1} with a MFPCA approach and the \mathbf{z}_{i2} with a classical PCA approach.

The first row of Figure 12 illustrates the estimated mean shape (in black) of the butterfly dataset, along with the effect of adding (in red) or subtracting (in blue) a multiple of the first three eigenfunctions resulting from the MFPCA. The last row presents the same curves for the fork dataset. This type of graph, inspired by (Ramsey and Silverman, 2005, Chap. 8), allows us to understand the sources of variability captured by the eigenfunctions.

For the butterfly dataset, the primary sources of variation are located in the antennae and wings. More specifically, the first eigenfunction captures variation in wing size proportional to body length, which represents the most significant source of variation among the butterflies in the dataset. The second and third eigenfunctions appear to capture variations in wing shape. This is particularly noticeable for the third eigenfunction, where a large value of the associated score leads to pointy wings, as shown in red.

For the fork dataset, the first eigenfunction captures a major source of variation: the fact that some forks have only three prongs instead of four, as seen in blue. The second eigenfunction captures variations in the overall fork shape, allowing for either elongated or bulkier forks, while the third eigenfunction captures variability in the handle shape.

Note that the first three eigenfunctions account for 65% of the total variance in the fork dataset, compared to 88% in the butterfly dataset, suggesting that the butterfly shapes have more dominant modes of variation compared to the forks.

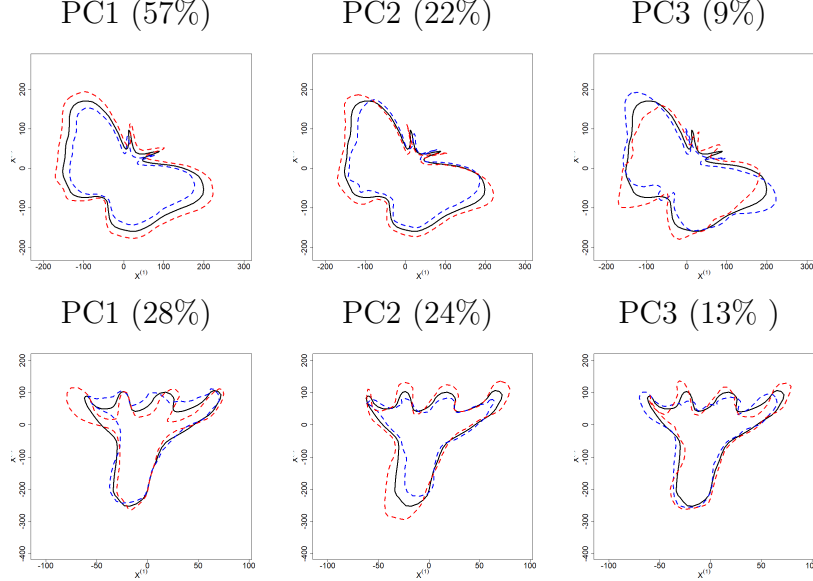


Figure 12: Plots of the estimated mean function $\bar{\mathbf{z}} = \sum_i \mathbf{z}_{i1}$ in black, of $\bar{\mathbf{z}} - 20\hat{\phi}_k$ in blue and of $\bar{\mathbf{z}} + 20\hat{\phi}_k$ in red, for $k = 1$ (first column), $k = 2$ (second column) and $k = 3$ (third column). The first row corresponds to the butterfly dataset, while the second row corresponds to the fork dataset. The number in parentheses in each plot title indicates the percentage of total variation explained by the corresponding eigenfunction.

To evaluate the ability of our joint PCA approach to model planar curves, we use the estimated model to generate new samples. The underlying idea is that a well-fitted model should produce realistic synthetic shapes that resemble those in the original datasets.

We define our generative model as presented in Section 3.2. Specifically, we simulate the score vectors $\boldsymbol{\xi} \in \mathbb{R}^{M_1 \times M_2}$ from the joint Gaussian model estimated from the data. Moreover, the number of retained principal components, M_1 associated with \mathbf{Z}_1 and M_2 associated with \mathbf{Z}_2 , is chosen such that the cumulative variance explained by the first M_1 eigenfunctions (resp. M_2 eigenvectors) reaches at least 90%. This results in setting $M_1 = 4$ and $M_2 = 4$ for the butterfly dataset and $M_1 = 7$ and $M_2 = 4$ for the fork dataset.

For comparison, we also generate new samples using an alternative approach: we use the estimated model obtained from applying the MFPCA method of Happ and Greven (2018) directly on the smoothed curves $\hat{\mathbf{x}}_i^s$, $i = 1, \dots, n_s$ and $s = b, f$. As before, we retain a number of principal components, denoted M_3 , such that the cumulative variance explained by the first M_3 components is at least of 90%. This leads to $M_3 = 3$ for the butterfly dataset and $M_3 = 4$ for the fork dataset. Note that this alternative approach does not explicitly model the deformation parameters, which may limit its ability to generate realistic curves.

Figures 13 and 14 illustrate examples of generated butterfly and fork curves, respectively. Each figure consists of three rows presenting five curves : row (a) shows curves generated with our approach without deformations, row (b) displays curves generated using our approach and with deformations, and row (c) presents curves generated with the MFPCA approach.

To assess numerically how well the generated curves resemble those in the original datasets, we introduce two similarity metrics based on the distance d defined in Section

2.2.2:

$$D_1(\mathbf{y}^s) = \frac{1}{n_s} \sum_{i=1}^{n_s} d(\mathbf{y}^{*s}, \hat{\mathbf{x}}_i^{*s}) \quad \text{and} \quad D_2(\mathbf{y}^s) = \min_{1 \leq i \leq n_s} d(\mathbf{y}^{*s}, \hat{\mathbf{x}}_i^{*s}),$$

where \mathbf{y}^s is a generated planar curve and \mathbf{y}^{*s} is its standardized shape with $s = b, f$.

A low value of $D_1(\mathbf{y}^s)$ indicates that the generated curve is on average close to the dataset's shapes, while a low value of $D_2(\mathbf{y}^s)$ indicates that at least one shape from the original dataset is similar to the generated one. The values of these two metrics for each generated curve are indicated at the top of each plot in Figures 13 and 14 .

Overall, our method produces more realistic shapes compared to the MFPCA approach. This is particularly evident in Figure 13, where the curves generated by our model (row (b)) closely resemble real butterfly silhouettes, whereas those from MFPCA (row (c)) tend to produce generic closed curves with little resemblance to actual butterflies.

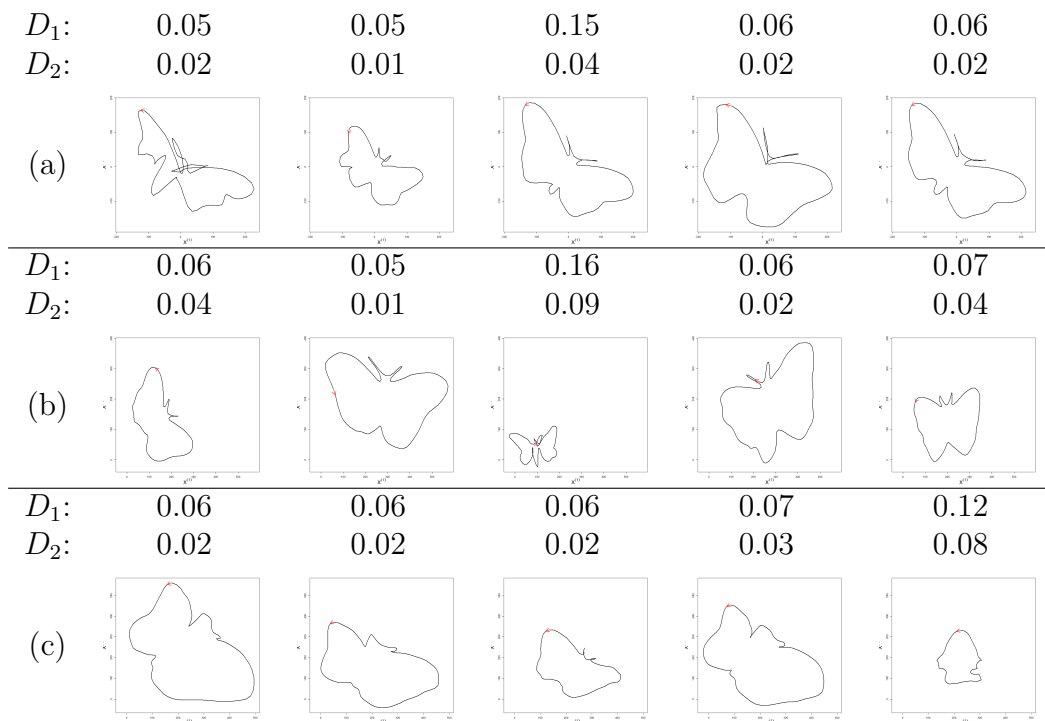


Figure 13: Butterfly curves generated with (a) our approach without the deformation parameters, (b) our approach with the deformation parameters, and (c) with MFPCA.

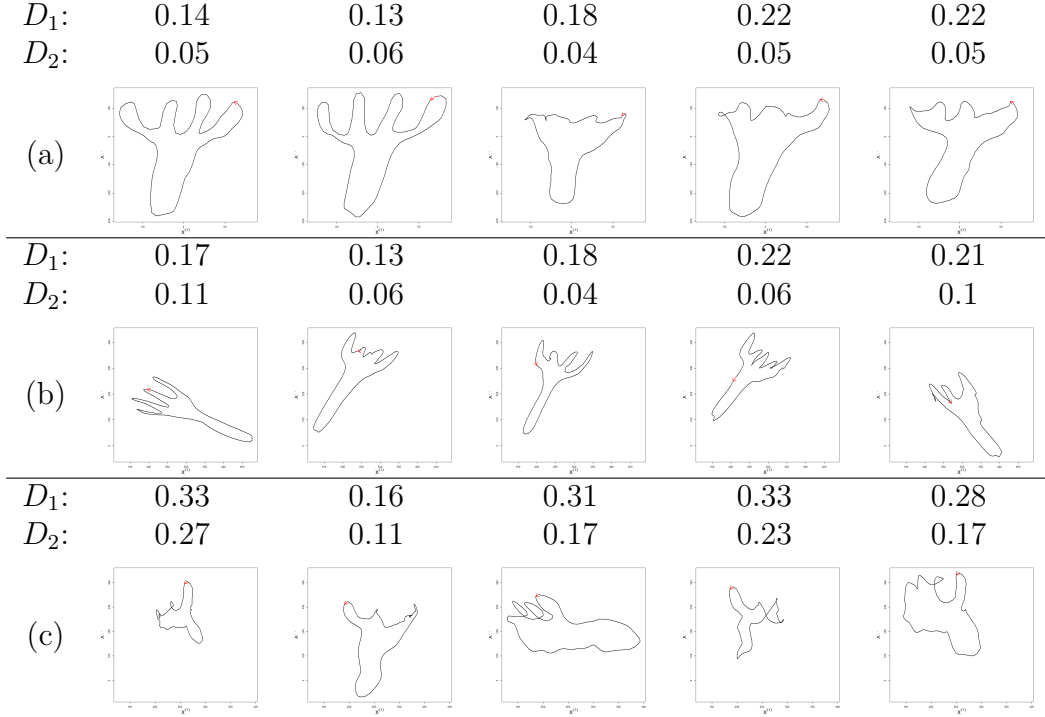


Figure 14: Fork curves generated with (a) our approach without the deformation parameters, (b) our approach with the deformation parameters, and (c) with MFPCA

6 Discussion

This paper addressed the study of random planar curves, with a particular focus on the contours of main silhouettes in images. The first part of our work deals with alignment, i.e., estimating the shape variable associated with a planar curve. To achieve this, we propose a suitable framework for determining the deformation variables. Once all the components of the planar curves are obtained, the second part introduces a novel model, inspired by functional data analysis, to account for their dependencies.

In the alignment step, since scaling and translation parameters can be easily obtained, our main focus was on estimating reparametrization and rotation deformations. We tackled this by defining an appropriate space for reparametrization functions and showing that the estimation problem then reduces to solving a Procrustes-like problem.

The model for random planar curves, introduced in the second part, is based on a joint principal component analysis. Specifically, it relies on the PCA of the "aligned" functional variable (the shape variable times the scaling factor) and the PCA of the remaining parameters of the planar curve (translation, rotation angle, and reparametrization function), mapped to a suitable multivariate representation.

A simulation study demonstrates the effectiveness of our framework in estimating the deformation variables under reasonable signal-to-noise ratios, as the obtained MSEs for the estimated parameters are close to zero. This is also confirmed by the real data application, where the estimated shape curves have similar coordinate functions. Moreover, the results from the real data analysis show that the generated shapes are more realistic compared to

those obtained with the classical MFPCA. This highlights the importance of aligning the planar curves before analyzing them.

A key aspect of our approach is the inclusion of deformation variables in the analysis, particularly the scaling parameter. This choice ensures that the functional space under study is linear, as it coincides with the space of closed curves. If the scaling parameter is considered as a nuisance parameter, the analysis has to be conducted on the unit sphere \mathbf{S}^∞ , where the shape variable resides. Since \mathbf{S}^∞ is a non-linear manifold, adapting our framework to this setting would require investigating common techniques in shape analysis, such as performing principal component analysis on the tangent space of \mathbf{S}^∞ (Dryden and Mardia (1998), Dai and Müller (2018)). Moreover, it is worth noting that alternative models for the rotation angle and starting point could be explored, by using their projection onto the unit circle, as they are circular variables (Mardia and Jupp, 2009).

Our work also presents some limitations. First, it focuses on the contour of the main object in an image, which may be restrictive in cases where multiple objects of interest are present in the same image. A possible extension would be to develop models for multiple planar curves. Additionally, the space of reparametrization functions considered in this paper accounts only for variations due to different starting points. While this assumption is reasonable for image contours, it may not hold in other settings where velocity changes occur. In such cases, an arc-length parametrization could be an interesting alternative, reducing all variations to the case we consider. Future work should explore this direction further.

A Additional figures

This section presents the results obtained from the analysis of the bat, horseshoe, and spoon datasets mentioned in Section 5. We applied the same procedure as for the butterfly and fork datasets, as described in Sections 5.1 and 5.2.

The results from the alignment procedure are illustrated in Figure 15. We observe that the obtained shapes and their corresponding coordinate functions are visually close to the function of reference $\boldsymbol{\mu}$. The case of the spoon dataset is particularly interesting: the bowl of the spoons is not always in the same position. This highlights an identifiability issue for certain shapes. However, their coordinate functions remain visually well-aligned.

The results related to the modeling of \mathbf{X} are shown in Figures 16, 17 and 18. Compared to the principal concurrent model (MFPCA), our proposed method generally produces more realistic shapes, especially for the bat and horseshoe datasets.

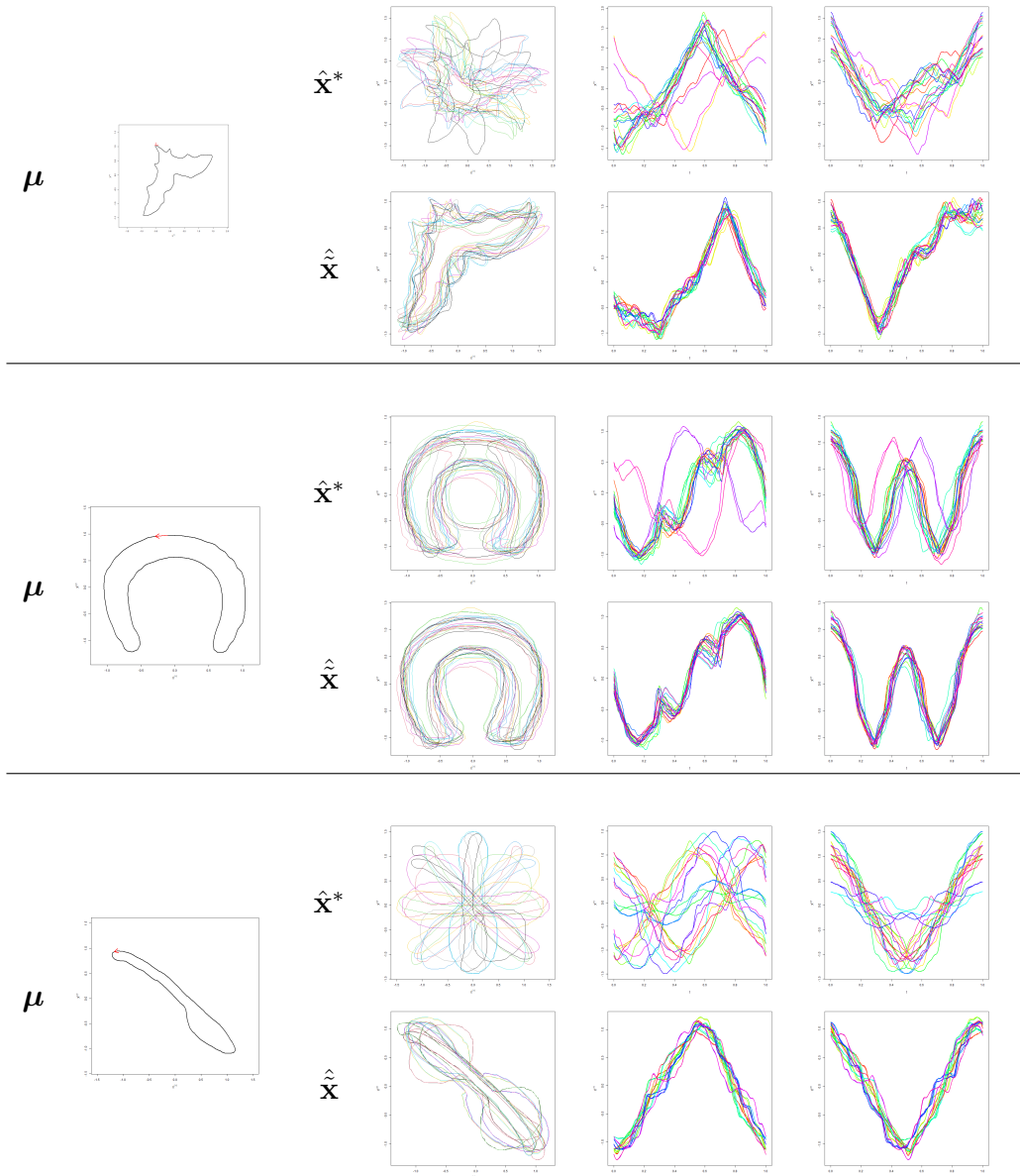


Figure 15: Illustration of the estimates of the standardized shapes (first row) and of the shapes (second) obtained from applying our alignment procedure to the bat (first block), horseshoe (second block) and spoon (third block) datasets.

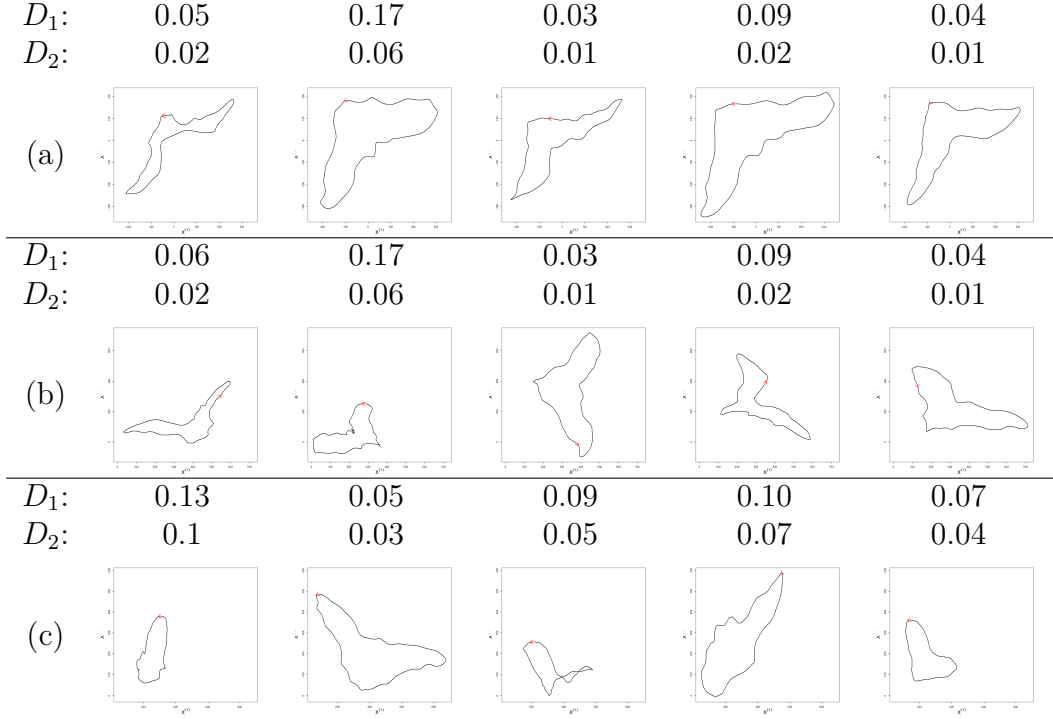


Figure 16: Bat curves generated with (a) our approach without the deformation parameters, (b) our approach with the deformation parameters, and (c) with MFPCA.

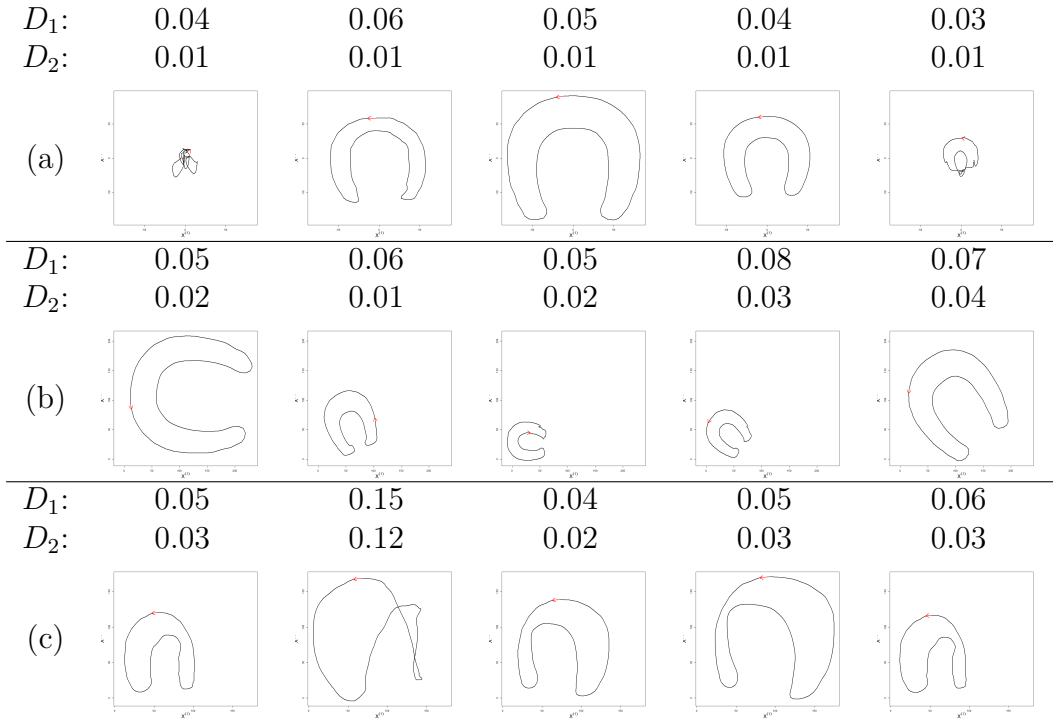


Figure 17: Horseshoe curves generated with (a) our approach without the deformation parameters, (b) our approach with the deformation parameters, and (c) with MFPCA.

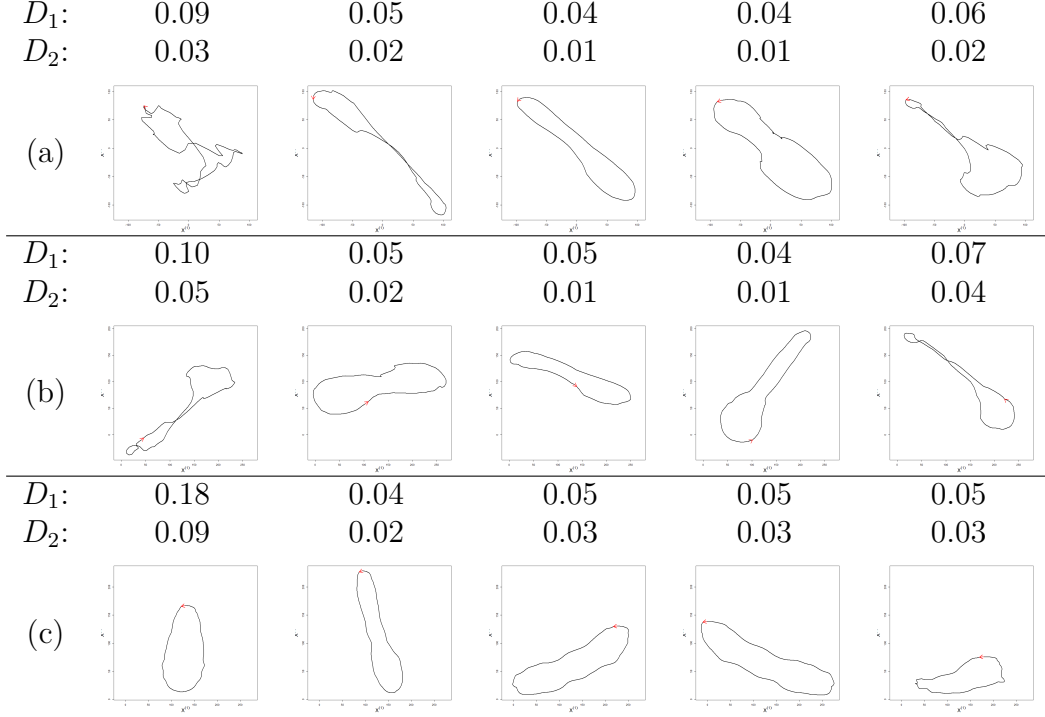


Figure 18: Spoon curves generated with (a) our approach without the deformation parameters, (b) our approach with the deformation parameters, and (c) with MFPCA.

B Proofs of the formal results

Proof of Proposition (2.1). The proposition is composed of two parts: (i) (Γ, \circ) is a group, and (ii) the isometry propriety holds.

Proof of (i): First recall that for $r \in \mathbb{R}$, we have that $\text{mod}(r, 1) = r - [r] \equiv \{r\}$, i.e., that $\{r\}$ is the fractional part of r . We use the following properties of the fractional part in the proof: (a) $\{\{r\}\} = \{r\}$, (b) $\{\{r_1\} + r_2\} = \{r_1 + r_2\}$, (c) $\{r + 1\} = \{r\}$ for $r, r_1, r_2 \in \mathbb{R}$, (d) $\{r\} = r - 1$ for $1 \leq r < 2$ and (e) $\{r\} = r + 1$ for $-1 \leq r < 0$.

The group structure is a consequence of the following lemma.

Lemma B.1. *Let $\gamma_{\delta_1}, \gamma_{\delta_2} \in \Gamma$, then*

$$\gamma_{\delta_1} \circ \gamma_{\delta_2} = \gamma_{\tilde{\delta}} \in \Gamma, \quad (14)$$

with $\tilde{\delta} = \text{mod}(\delta_1 + \delta_2, 1)$.

Proof. First note that by definition $\gamma_0 = \text{mod}(t, 1) = \text{mod}(t - 1, 1) = \gamma_1$.

- **Case where $\delta_1 \in \{0, 1\}$ and/or $\delta_2 \in \{0, 1\}$.** If $\delta_1 = 0$ and $\delta_2 \in [0, 1]$, then for any

$t \in [0, 1]$, we have

$$\begin{aligned}
\gamma_{\delta_1} \circ \gamma_{\delta_2}(t) &= \gamma_0 \circ \gamma_{\delta_2}(t) = \text{mod}(\gamma_{\delta_2}(t), 1) = \text{mod}(\text{mod}(t - \delta_2, 1), 1) \\
&= \text{mod}(t - \delta_2, 1) \\
&= \begin{cases} \gamma_{\delta_2} & \text{if } \delta_2 < 1 \\ \gamma_0 & \text{if } \delta_2 = 1 \end{cases} \\
&= \gamma_{\text{mod}(0+\delta_2,1)}.
\end{aligned}$$

All the other cases are shown with a similar argument.

- **Case where $\delta_1 \in (0, 1)$ and $\delta_2 \in (0, 1)$.** For any $t \in [0, 1]$ we have

$$\gamma_{\delta_2}(t) = \begin{cases} 1 + (t - \delta_2) & \text{if } t - \delta_2 < 0, \\ (t - \delta_2) & \text{if } t - \delta_2 \geq 0, \end{cases}$$

which leads to

$$\begin{aligned}
\gamma_{\delta_1} \circ \gamma_{\delta_2}(t) &= \text{mod}(\gamma_{\delta_2}(t) - \delta_1, 1) \\
&= \begin{cases} \text{mod}(1 + (t - \delta_2) - \delta_1, 1) & \text{if } t - \delta_2 < 0 \\ \text{mod}((t - \delta_2) - \delta_1, 1) & \text{if } t - \delta_2 \geq 0 \end{cases} \\
&= \text{mod}(t - (\delta_2 + \delta_1), 1) \\
&= \text{mod}(t - \tilde{\delta}, 1).
\end{aligned}$$

The last equality comes from the fact that

$$\delta_1 + \delta_2 = \begin{cases} \tilde{\delta} & \text{if } \delta_1 + \delta_2 < 1 \\ \tilde{\delta} + 1 & \text{if } \delta_1 + \delta_2 \geq 1 \end{cases}, \quad \text{and} \quad \text{mod}(t - \tilde{\delta}, 1) = \text{mod}(t - (\tilde{\delta} + 1), 1).$$

Since by definition $\tilde{\delta} \in [0, 1)$, we finally have that $\gamma_{\delta_1} \circ \gamma_{\delta_2}(t) = \text{mod}(t - \tilde{\delta}, 1) = \gamma_{\tilde{\delta}}(t)$, with $\gamma_{\tilde{\delta}} \in \Gamma$.

□

The proof that (Γ, \circ) is a group follows directly from Lemma B.1 :

- **Associativity:** Let $\gamma_{\delta_1}, \gamma_{\delta_2}, \gamma_{\delta_3} \in \Gamma$, then we have

$$\begin{aligned}
(\gamma_{\delta_1} \circ \gamma_{\delta_2}) \circ \gamma_{\delta_3} &= \gamma_{\text{mod}(\delta_1+\delta_2,1)} \circ \gamma_{\delta_3} \\
&= \gamma_{\text{mod}(\text{mod}(\delta_1+\delta_2,1)+\delta_3,1)} \\
&= \gamma_{\text{mod}(\delta_1+\text{mod}(\delta_2+\delta_3,1),1)} \\
&= \gamma_{\delta_1} \circ (\gamma_{\delta_2} \circ \gamma_{\delta_3}),
\end{aligned}$$

where we used property (b) of fractional parts to obtain the third equality.

- **Identity element:** The function $\gamma_0 \in \Gamma$ is the identity element since for any $\gamma_{\delta} \in \Gamma$, we have

$$\gamma_{\delta} \circ \gamma_0 = \gamma_0 \circ \gamma_{\delta} = \gamma_{\text{mod}(\delta+0,1)} = \gamma_{\delta}.$$

- **Inverse element:** Let $\gamma_{\delta} \in \Gamma$ then $\gamma_{1-\delta} \in \Gamma$ is the inverse of γ_{δ} since

$$\gamma_{\delta} \circ \gamma_{1-\delta} = \gamma_{\text{mod}(\delta+(1-\delta),1)} = \gamma_0 \quad \text{and} \quad \gamma_{1-\delta} \circ \gamma_{\delta} = \gamma_{\text{mod}(1-\delta)+\delta,1)} = \gamma_0.$$

This concludes the proof of (i).

Proof of (ii): Let $\mathbf{f} = (f^{(1)}, f^{(2)})^\top \in \mathcal{H}$ and $\gamma_\delta \in \Gamma$, we have that

$$\|\mathbf{f} \circ \gamma_\delta\|_2^2 = \int_0^1 (f^{(1)} \circ \gamma_\delta(t))^2 dt + \int_0^1 (f^{(2)} \circ \gamma_\delta(t))^2 dt,$$

where for $j \in \{1, 2\}$ and $t \in (0, 1)$, we have

$$f^{(j)} \circ \gamma_\delta(t) = \begin{cases} f^{(j)}(1+t-\delta) & \text{if } t-\delta < 0, \\ f^{(j)}(t-\delta) & \text{if } t-\delta \geq 0. \end{cases}$$

Then

$$\begin{aligned} \int_0^1 (f^{(j)} \circ \gamma_\delta(t))^2 dt &= \int_0^\delta (f^{(j)}(1+t-\delta))^2 dt + \int_\delta^1 (f^{(j)}(t-\delta))^2 dt \\ &= \int_{1-\delta}^1 (f^{(j)}(u))^2 du + \int_0^{1-\delta} (f^{(j)}(u))^2 du \\ &= \int_0^1 (f^{(j)}(u))^2 du, \end{aligned}$$

which leads to

$$\|\mathbf{f} \circ \gamma_\delta\|_2^2 = \int_0^1 (f^{(1)}(u))^2 du + \int_0^1 (f^{(2)}(u))^2 du = \|\mathbf{f}\|_2^2.$$

□

Proof of Lemma 2.2. Let $\mathbf{f}, \mathbf{g} \in \mathcal{H}$.

- **Positivity:** We have by definition

$$d(\mathbf{f}, \mathbf{g}) = \min_{\delta \in [0,1], \theta \in [0,2\pi]} \|\mathbf{f} \circ \gamma_\delta - \mathbf{O}_\theta \mathbf{g}\|_{\mathcal{H}} \geq 0,$$

and

$$d(\mathbf{f}, \mathbf{f}) = \min_{\delta \in [0,1], \theta \in [0,2\pi]} \|\mathbf{f} \circ \gamma_\delta - \mathbf{O}_\theta \mathbf{f}\|_{\mathcal{H}} = \|\mathbf{f} \circ \gamma_0 - \mathbf{O}_0 \mathbf{f}\|_{\mathcal{H}} = 0.$$

- **Symmetry:** First note that

$$d(\mathbf{f}, \mathbf{g}) = \min_{\delta \in [0,1], \theta \in [0,2\pi]} \|\mathbf{f} \circ \gamma_\delta - \mathbf{O}_\theta \mathbf{g}\|_{\mathcal{H}} = \min_{\delta \in [0,1], \theta \in [0,2\pi]} \|\mathbf{O}_{2\pi-\theta} \mathbf{f} - \mathbf{g} \circ \gamma_{1-\delta}\|_{\mathcal{H}}.$$

Letting $\theta' = 2\pi - \theta$ and $\delta' = 1 - \delta$, we have that

$$d(\mathbf{f}, \mathbf{g}) = \min_{\delta' \in [0,1], \theta' \in [0,2\pi]} \|\mathbf{O}_{\theta'} \mathbf{f} - \mathbf{g} \circ \gamma_{\delta'}\|_{\mathcal{H}} = d(\mathbf{g}, \mathbf{f}).$$

- **Triangle inequality:**

Since $\|\cdot\|_{\mathcal{H}}$ induce a proper distance, we have that

$$\|\mathbf{f}_1 - \mathbf{f}_2\|_{\mathcal{H}} + \|\mathbf{f}_2 - \mathbf{f}_3\|_{\mathcal{H}} \geq \|\mathbf{f}_1 - \mathbf{f}_3\|_{\mathcal{H}}$$

for $\mathbf{f}_1, \mathbf{f}_2, \mathbf{f}_3 \in \mathcal{H}$.

For any $\mathbf{f}, \mathbf{r}, \mathbf{g} \in \mathcal{H}$, by letting $\mathbf{f}_1 = \mathbf{f} \circ \gamma_\delta$, $\mathbf{f}_2 = \mathbf{O}_\theta \mathbf{r}$ and $\mathbf{f}_3 = \mathbf{O}_{\theta'} \mathbf{g} \circ \gamma_{\delta'}$ in the previous inequality, we obtain

$$\begin{aligned} & \|\mathbf{f} \circ \gamma_\delta - \mathbf{O}_\theta \mathbf{r}\|_{\mathcal{H}} + \|\mathbf{O}_\theta \mathbf{r} - \mathbf{O}_{\theta'} \mathbf{g} \circ \gamma_{\delta'}\|_{\mathcal{H}} \geq \|\mathbf{f} \circ \gamma_\delta - \mathbf{O}_{\theta'} \mathbf{g} \circ \gamma_{\delta'}\|_{\mathcal{H}} \\ & \Rightarrow \min_{\delta, \delta' \in [0, 1], \theta, \theta' \in [0, 2\pi]} (\|\mathbf{f} \circ \gamma_\delta - \mathbf{O}_\theta \mathbf{r}\|_{\mathcal{H}} + \|\mathbf{O}_\theta \mathbf{r} - \mathbf{O}_{\theta'} \mathbf{g} \circ \gamma_{\delta'}\|_{\mathcal{H}}) \\ & \geq \min_{\delta, \delta' \in [0, 1], \theta, \theta' \in [0, 2\pi]} \|\mathbf{f} \circ \gamma_\delta - \mathbf{O}_{\theta'} \mathbf{g} \circ \gamma_{\delta'}\|_{\mathcal{H}}. \end{aligned} \quad (15)$$

The left-hand side of the inequality (15) admits the following simplification

$$\begin{aligned} & \min_{\delta, \delta' \in [0, 1], \theta, \theta' \in [0, 2\pi]} (\|\mathbf{f} \circ \gamma_\delta - \mathbf{O}_\theta \mathbf{r}\|_{\mathcal{H}} + \|\mathbf{O}_\theta \mathbf{r} - \mathbf{O}_{\theta'} \mathbf{g} \circ \gamma_{\delta'}\|_{\mathcal{H}}) \\ & = \min_{\delta, \delta' \in [0, 1], \theta, \theta' \in [0, 2\pi]} (\|\mathbf{f} \circ \gamma_\delta - \mathbf{O}_\theta \mathbf{r}\|_{\mathcal{H}} + \|\mathbf{r} - \mathbf{O}_{\theta' - \theta} \mathbf{g} \circ \gamma_{\delta'}\|_{\mathcal{H}}) \\ & = \min_{\delta \in [0, 1], \theta \in [0, 2\pi]} (\|\mathbf{f} \circ \gamma_\delta - \mathbf{O}_\theta \mathbf{r}\|_{\mathcal{H}}) + \min_{\delta' \in [0, 1], \theta^* \in [0, 2\pi]} (\|\mathbf{r} - \mathbf{O}_{\theta^*} \mathbf{g} \circ \gamma_{\delta'}\|_{\mathcal{H}}), \end{aligned}$$

where

$$\min_{\delta \in [0, 1], \theta \in [0, 2\pi]} \|\mathbf{f} \circ \gamma_\delta - \mathbf{O}_\theta \mathbf{r}\|_{\mathcal{H}} = d(\mathbf{f}, \mathbf{r}),$$

and

$$\min_{\delta' \in [0, 1], \theta^* \in [0, 2\pi]} \|\mathbf{r} - \mathbf{O}_{\theta^*} \mathbf{g} \circ \gamma_{\delta'}\|_{\mathcal{H}} = \min_{\delta' \in [0, 1], \theta^* \in [0, 2\pi]} \|\mathbf{r} \circ \gamma_{1-\delta'} - \mathbf{O}_{\theta^*} \mathbf{g}\|_{\mathcal{H}} = d(\mathbf{r}, \mathbf{g}).$$

Using a similar reasoning, we can show that the right-hand side of (15) is equal to $d(\mathbf{f}, \mathbf{g})$, and thus that $d(\mathbf{f}, \mathbf{r}) + d(\mathbf{r}, \mathbf{g}) \geq d(\mathbf{f}, \mathbf{g})$. □

Proof of Lemma (2.3). Due to the block structure of the matrix $\beta(\delta)$, the lemma follows directly from the fact that

$$\begin{pmatrix} \sin(2m\pi\gamma_\delta(t)) \\ \cos(2m\pi\gamma_\delta(t)) \end{pmatrix} = \mathbf{O}_{-2m\pi\delta} \begin{pmatrix} \sin(2m\pi t) \\ \cos(2m\pi t) \end{pmatrix}, \quad (16)$$

for $m \in \mathbb{N}^*$ and $\gamma_\delta \in \Gamma$, which we prove below.

First note that for $t \in [0, 1]$,

$$\sin(2m\pi\gamma_\delta(t)) = \begin{cases} \sin(2m\pi(t - \delta)) & t \leq \delta \\ \sin(2m\pi((t - \delta) - 1)) & t > \delta, \end{cases}$$

where $\sin(2m\pi((t - \delta) - 1)) = \sin(2\pi(t - \delta) - 2m\pi) = \sin(2\pi(t - \delta))$. Hence

$$\sin(2m\pi\gamma_\delta(t)) = \sin(2m\pi(t - \delta)).$$

The same reasoning shows that

$$\cos(2m\pi\gamma_\delta(t)) = \cos(2m\pi(t - \delta)).$$

Finally,

$$\begin{pmatrix} \sin(2m\pi\gamma_\delta(t)) \\ \cos(2m\pi\gamma_\delta(t)) \end{pmatrix} = \begin{pmatrix} \sin(2m\pi t - 2m\pi\delta) \\ \cos(2m\pi t - 2m\pi\delta) \end{pmatrix} = \mathbf{O}_{-2m\pi\delta} \begin{pmatrix} \sin(2m\pi t) \\ \cos(2m\pi t) \end{pmatrix},$$

which concludes the proof. \square

Proof of Proposition (2.4). Let $\mathbf{f}_{\theta,\delta} = \mathbf{X}^* - \mathbf{O}_\theta \boldsymbol{\mu} \circ \gamma_\delta$, this function admits the following representation

$$\mathbf{f}_{\theta,\delta} = \begin{pmatrix} \boldsymbol{\psi}^\top & 0 \\ 0 & \boldsymbol{\psi}^\top \end{pmatrix} \bar{\boldsymbol{\alpha}}_{\theta,\delta},$$

with

$$\bar{\boldsymbol{\alpha}}_{\theta,\delta} = \text{Vec} \left((\boldsymbol{\alpha}\boldsymbol{\beta}(\delta) - \mathbf{O}_\theta \mathbf{u})^\top \right),$$

and where $\text{Vec}(\cdot)$ is the vectorization operator. Hence the norm of $\mathbf{f}_{\theta,\delta}$ is given by

$$\begin{aligned} \|\mathbf{f}_{\theta,\delta}\|_{\mathcal{H}}^2 &= \int_0^1 \mathbf{f}_{\theta,\delta}^\top(t) \mathbf{f}_{\theta,\delta}(t) dt \\ &= \bar{\boldsymbol{\alpha}}_{\theta,\delta}^\top \underbrace{\left[\int_0^1 \begin{pmatrix} \boldsymbol{\psi}(t) & 0 \\ 0 & \boldsymbol{\psi}(t) \end{pmatrix} \begin{pmatrix} \boldsymbol{\psi}^\top(t) & 0 \\ 0 & \boldsymbol{\psi}^\top(t) \end{pmatrix} dt \right]}_{\mathbf{I}} \bar{\boldsymbol{\alpha}}_{\theta,\delta} \\ &= \bar{\boldsymbol{\alpha}}_{\theta,\delta}^\top \bar{\boldsymbol{\alpha}}_{\theta,\delta} \\ &= \|\bar{\boldsymbol{\alpha}}_{\theta,\delta}\|_2^2 \\ &= \left\| \text{Vec} \left((\boldsymbol{\alpha}\boldsymbol{\beta}(\delta) - \mathbf{O}_\theta \mathbf{u})^\top \right) \right\|_2^2 \\ &= \|\boldsymbol{\alpha}\boldsymbol{\beta}(\delta) - \mathbf{O}_\theta \mathbf{u}\|_F^2, \end{aligned}$$

which concludes the proof. \square

References

- Bradski, G. (2000). The OpenCV Library. *Dr. Dobb's Journal of Software Tools*.
- Burger, W. and Burge, M. J. (2009). *Principles of digital image processing*, volume 111. Springer.
- Carlier, A., Leonard, K., Hahmann, S., Morin, G., and Collins, M. (2016). The 2d shape structure dataset: A user annotated open access database. *Computers & Graphics*, 58:23–30.
- Dai, X. (2022). Statistical inference on the hilbert sphere with application to random densities. *Electronic Journal of Statistics*, 16(1):700–736.
- Dai, X. and Müller, H.-G. (2018). Principal component analysis for functional data on riemannian manifolds and spheres. *The Annals of Statistics*, 46(6B):3334–3362.
- Dryden, I. L. and Mardia, K. V. (1998). *Statistical analysis of shape*. Wiley.
- Happ, C. and Greven, S. (2018). Multivariate functional principal component analysis for data observed on different (dimensional) domains. *Journal of the American Statistical Association*, 113(522):649–659.
- Happ, C., Scheipl, F., Gabriel, A.-A., and Greven, S. (2019). A general framework for multivariate functional principal component analysis of amplitude and phase variation. *Stat*, 8(1):e220.
- Jacques, J. and Preda, C. (2014). Model-based clustering for multivariate functional data. *Computational Statistics & Data Analysis*, 71:92–106.
- Kendall, D. G. (1989). A survey of the statistical theory of shape. *Statistical Science*, 4(2):87–99.
- Mardia, K. V. and Jupp, P. E. (2009). *Directional statistics*. John Wiley & Sons.
- Marron, J. S., Ramsay, J. O., Sangalli, L. M., and Srivastava, A. (2015). Functional data analysis of amplitude and phase variation. *Statistical Science*, pages 468–484.
- nl, C. (2020). Flying grey long eared bat isolated on white background stock photo. <https://www.istockphoto.com/photo/>.
- Oussidi, A. and Elhassouny, A. (2018). Deep generative models: Survey. In *2018 International conference on intelligent systems and computer vision (ISCV)*, pages 1–8. IEEE.
- Ramsey, J. O. and Silverman, B. W. (2005). *Functional Data Analysis*. Springer New York, 2nd edition.
- Schönemann, P. H. (1966). A generalized solution of the orthogonal procrustes problem. *Psychometrika*, 31(1):1–10.

- Srivastava, A., Klassen, E., Joshi, S. H., and Jermyn, I. H. (2010). Shape analysis of elastic curves in euclidean spaces. *IEEE transactions on pattern analysis and machine intelligence*, 33(7):1415–1428.
- Srivastava, A. and Klassen, E. P. (2016). *Functional and shape data analysis*, volume 1. Springer.
- Stöcker, A., Steyer, L., and Greven, S. (2023). Functional additive models on manifolds of planar shapes and forms. *Journal of Computational and Graphical Statistics*, 32(4):1600–1612.
- Tucker, J. D. (2023). *fdasrvf: Elastic Functional Data Analysis*. R package version 2.0.4.
- Tucker, J. D., Wu, W., and Srivastava, A. (2013). Generative models for functional data using phase and amplitude separation. *Computational Statistics & Data Analysis*, 61:50–66.
- Weisstein, E. W. (2003). Heart curve. <https://mathworld.wolfram.com/>.
- Younes, L. (1998). Computable elastic distances between shapes. *SIAM Journal on Applied Mathematics*, 58(2):565–586.